PTEP

Prog. Theor. Exp. Phys. **2018**, 113D01 (32 pages)
DOI: 10.1093/ptep/pty110

Hypernuclear non-mesonic weak decays in the extended meson exchange model

Kazunori Itonaga[1,*], Toshio Motoba[2,3], and Thomas A. Rijken[4]

[1]*Physics Department, Gifu University, 1-1 Yanagido, Gifu 501-1192, Japan*
[2]*Laboratory of Physics, Osaka Electro-Communication University, Neyagawa 572-8530, Japan*
[3]*Yukawa Institute for Theoretical Physics, Kyoto University, Kyoto 606-8502, Japan*
[4]*Institute of Mathematics, Astrophysics, and Particle Physics, University of Nijmegen, Nijmegen, The Netherlands*
[*]E-mail: kazunori.itonaga@gmail.com

Received June 23, 2018; Revised September 13, 2018; Accepted September 26, 2018; Published November 24, 2018

An extended meson exchange model for the $\Lambda N \to NN$ weak decay interactions is presented by taking full account of the pseudoscalar, vector, scalar, and axial-vector meson exchanges, as well as the pomeron exchange. In the procedure we make use of the strong coupling constants for baryon–baryon–meson vertices of the Nijmegen ESC08c model (2016 version). The present model can explain satisfactorily the hypernuclear non-mesonic weak decay observables such as decay rates $\Gamma_{\rm nm}$, Γ_n/Γ_p, asymmetry parameters α_Λ, and lifetimes τ for light-to-heavy mass systems. Attention is payed to the proper roles of each meson exchange. In the parity-conserving channels, the potentials due to the non-strange mesons (π, ρ, a_1) are found to behave oppositely in signs to the potentials due to the strange mesons (K, K^*, K_1) having the same $J^{\rm PC}$, respectively. In the parity-violating part, all the weak potentials work additively in the ${}^3S_1 \to {}^1P_1$ channel. We found that the one-nucleon-induced non-mesonic weak decays proceed predominantly through the parity-violating $({}^3S_1)_{\Lambda N} \to ({}^1P_1)_{NN}$ and $({}^3S_1)_{\Lambda N} \to ({}^3P_1)_{NN}$ channels.

Subject Index D02, D14, D29

1. Introduction

As the hyperon–nucleon (YN) scattering experiment in free space is practically impossible, the hypernucleus, which is a strongly interacting many-body system consisting of nucleons and hyperon(s), offers us a nice laboratory for the study of the strangeness $S = -1$ sector of baryon–baryon strong interactions. The behavior of the Pauli-free hyperon in the nuclear medium is also a novel subject which attracts many theoretical and experimental interests [1–5]. When the Λ hypernucleus is produced by K, π, and electron beams or in heavy-ion collisions, it is mostly in the excited state and is polarized depending on the reaction kinematics [6–8]. The hypernucleus de-excites and cascades down by emitting γ rays and/or nucleon(s) through electromagnetic or strong interactions until it reaches the ground state.

The Λ hypernucleus eventually decays through strangeness-changing ($\Delta S = 1$) weak interactions to form non-strange final nuclear particles. The hypernuclear lifetime is of the order of that of the Λ particle itself ($\tau_\Lambda = 2.63 \times 10^{-10}$ s). Thus the hypernuclear weak process offers another nice opportunity for the study of hyperon–nucleon weak interaction. The weak decay process consists of the π-mesonic mode and the non-mesonic (NM) mode, where the former process has been explained well theoretically [9,10]. On the other hand, hypernuclear NM weak decay has attracted much attention because the experimental phenomena are not always easy to understand and also

because the non-mesonic weak decay interactions were not fully established. Much NM weak decay data have been accumulated along with the development of experimental facilities and innovative detection techniques. Those data include the total non-mesonic decay rates, the partial decay rates for the processes such as $\Lambda p \to np$, $\Lambda n \to nn$, and two-nucleon-induced ones, the decay proton and neutron spectra, the asymmetry parameters of the decay proton angular distribution from the polarized hypernuclei, and the hypernuclear lifetimes [5,11–18].

On the theoretical side, much work has been performed over several decades by focusing attention on how to theoretically construct the NM weak decay interactions between Λ and nucleons. Those efforts include the various meson exchange models [10,19–26], the quark–meson hybrid model [27,28], and the effective field theory [29,30]. We note here that the meson-exchange potentials by Chumillas et al. [23] are successful in explaining the $\Gamma_{\rm nm}$, Γ_n/Γ_p, and the asymmetry parameter data of ${}^{5}_{\Lambda}$He and ${}^{12}_{\Lambda}$C weak decays. It is essential for any theory that the NM weak decay observables such as the total decay rate $\Gamma_{\rm nm}$, the partial decay ratio Γ_n/Γ_p, and the asymmetry parameter of decay protons should be explained consistently.

In the course of our study of NM weak decay [10,25,26], we have proposed a framework to take into account the correlated two-meson/meson exchange processes in constructing the weak decay interaction between Λ and N. In fact, in addition to the one-meson exchanges, we have tried to include the $2\pi/\rho$ and $2\pi/\sigma$ exchanges [25] for the first time and then extended further to take the axial-vector a_1 exchanges such as $\rho\pi/a_1$ and $\sigma\pi/a_1$ [10,26], showing that the data of $\Gamma_{\rm nm}$, Γ_n/Γ_p, and the asymmetry parameters of s- and p-shell hypernuclei can be explained. It should be emphasized first that the framework has an important merit of flexibility in treating various kinds of correlated two-meson exchanges. Also, one can extend the construction of weak interactions corresponding to the development of the strong baryon–baryon forces.

Recently, a new version of the Nijmegen extended-soft-core model called ESC08c has been proposed to describe the strong NN and hyperon–nucleon YN as well as hyperon–hyperon interactions in a unified way using the broken SU(3) symmetry [31–33]. The strong potentials include contributions from one-boson exchanges of the nonet meson members such as pseudoscalar, vector, scalar, and axial-vector mesons, and the diffractive exchanges; their parameters have been determined on the basis of the NN and YN scattering data and the updated hypernuclear structure data with strangeness $S = -1$ and -2. This new version of the strong interactions provides us another opportunity to study the roles of various meson exchanges in the extended weak NM decay Hamiltonian. On the other hand, new experimental weak decay data have been reported from the FINUDA experiments [4,13,14] on the proton-stimulated decay rate $\Gamma_p(\Lambda p \to np)$ for $A = 5$–16 mass hypernuclei and the neutron-stimulated decay rate $\Gamma_n(\Lambda p \to nn)$ for some hypernuclei, and also on the two-nucleon-induced decay ratios $\Gamma_{2N}/\Gamma_{\rm nm}$ for these hypernuclei. New lifetime data for medium-heavy hypernuclei were reported quite recently [34].

In view of this situation we think it timely to achieve an essential update in constructing the weak NM decay interactions by extending our previous framework as employed in Refs. [10,25,26]. This is the first purpose of this paper. In order to maintain this aim, the weak decay meson exchanges are consistently introduced in a wider and firm basis under the following guidelines.

(1) Exchange mesons are considered to cover the quantum numbers of pseudoscalar ($J^{\rm PC} = 0^{-+}$), vector ($J^{\rm PC} = 1^{--}$), scalar ($J^{\rm PC} = 0^{++}$), and axial-vector ($J^{\rm PC} = 1^{++}$, first kind) types, and the model should include the pomeron ($J^{\rm PC} = 0^{++}$) exchange as well.
(2) Non-strange mesons and strange mesons are considered equally and symmetrically.

(3) The new baryon–baryon–meson coupling constants from the ESC08c model [32,33] are employed for strong vertices in the weak decay diagrams.

As the second purpose of this paper, we clarify the roles of the various meson exchanges as well as the pomeron exchange and evaluate their contributions to the NM weak potentials and the weak decay observables. In addition, we will analyze the decay characteristics of the non-mesonic weak decays by investigating the six decay channels starting from the initial ΛN relative S-state.

In Sect. 2, the formulas of the non-mesonic weak decay rate and the asymmetry parameter are given. The weak decay transition potentials for $\Lambda N \to NN$ are constructed in the extended meson exchange model in Sect. 3. Calculated non-mesonic weak decay potentials are presented in Sect. 4. In Sect. 4.1, the initial hypernuclear states and final nuclear and outgoing two-nucleon states are described. In Sect. 4.2, the weak decay potentials of six decay channels are displayed to see the roles of each meson-exchange potential. Then the potential properties based on the pseudoscalar and vector meson exchanges are discussed in Sect. 4.3, and those based on the scalar and axial-vector mesons and pomeron exchanges are discussed in Sect. 4.4. In Sect. 5 the calculated weak decay observables are shown and compared with the experimental data. Calculations are carried out step by step by adding the meson exchange potentials successively to elucidate the effects of potentials on the decay observables. These matters are presented through Sects. 5.1–5.3. Also, the relation between the model by Chumillas et al. [23] and our present model is discussed in Sect. 5.4. Finally, a summary and conclusions are given in Sect. 6. In Appendix A the expression for the NM decay rate Γ_1 is given. The definitions of meson-decay coupling interactions are described in Appendix B.

2. Formulas for non-mesonic weak decay rates and asymmetry parameter

The hypernucleus, as a strongly interacting system of nucleons and hyperon(s) with strangeness, finally decays through the weak non-leptonic process of either the mesonic mode or the non-mesonic mode, leaving a non-strange residual nucleus.

In this paper we confine ourselves to study the one-nucleon-induced non-mesonic decays such as $\Lambda p \to np$ and $\Lambda n \to nn$. Formulas for the non-mesonic decay rates and the asymmetry parameter have been presented in the previous papers [10,26], but a brief recapitulation of these expressions would be appropriate for later discussions.

The hypernuclear non-mesonic decay rate $\Gamma_{\rm nm}$ is evaluated by using the unpolarized density matrix $\rho_{\rm unpol}$ as follows:

$$\Gamma_{\rm nm} = {\rm Tr}\,(T \rho_{\rm unpol} T^\dagger), \tag{1}$$

$$\rho_{\rm unpol} = \frac{1}{2J_H+1}\,1, \tag{2}$$

where T is the transition matrix from the initial hypernuclear state (J_H, T_H) to the final residual nuclear plus outgoing two-nucleon state. Thus the non-mesonic weak decay rate is given by summing all the final states of the process ${}^A_\Lambda{\rm Z}\,(J_H, T_H) \to {}^{A-2}{\rm Z}'\,(J'_1, T'_1) + N + N$ as

$$\begin{aligned}\Gamma_{\rm nm} = {} & \frac{2\pi}{2J_H+1} \sum_{J'_1 M'_1 \alpha'_1} \sum_{T'_1 M'_{T_1}} \sum_{S'_2 M'_{S_2}} \sum_{T'_2 M'_{T_2}} \sum_{M_H} \int \frac{d\boldsymbol{k}}{(2\pi)^3} \int \frac{d\boldsymbol{K}}{(2\pi)^3}\, \delta(E_f - E_i) \\ & \times \left| \left\langle {}^{A-2}\Phi_{J'_1 M'_1 \alpha'_1, T'_1 M'_{T_1}} \frac{1}{\sqrt{2}} [1 - (-1)^{S'_2+T'_2} P_x]\, e^{i\boldsymbol{k}\cdot\boldsymbol{r}} e^{i\boldsymbol{K}\cdot\boldsymbol{R}} \right.\right. \\ & \left.\left. \times\ \chi^{S'_2}_{M'_{S_2}} \xi^{T'_2}_{M'_{T_2}} \mid \sum_{ik} V_{\rm nm}(i,k) \mid {}^A_\Lambda\Psi\,; J_H M_H,\ T_H M_{T_H} \right\rangle \right|^2 . \end{aligned} \tag{3}$$

Here, $V_{\rm nm}(i,k)$ is the $\Lambda N \to NN$ weak decay interaction. P_x signifies an exchange operator for the outgoing two nucleon radial vectors. The relative and the center-of-mass radial vectors and the corresponding momenta are defined, respectively, as

$$\boldsymbol{r} = \boldsymbol{r}_1 - \boldsymbol{r}_2, \quad \boldsymbol{R} = \frac{\boldsymbol{r}_1 + \boldsymbol{r}_2}{2}, \tag{4}$$

$$\boldsymbol{k} = \frac{\boldsymbol{k}_1 - \boldsymbol{k}_2}{2}, \quad \boldsymbol{K} = \boldsymbol{k}_1 + \boldsymbol{k}_2. \tag{5}$$

The energy conservation δ-function is expressed as

$$\delta(E_f - E_i) = \delta\left(\frac{\boldsymbol{k}^2}{M_N} + \frac{\boldsymbol{K}^2}{4M_N} + E_x(A-2, J'_1 T'_1 \alpha'_1) + \frac{\boldsymbol{K}^2}{2M_{A-2}} + M_N - M_\Lambda - \varepsilon_N - \varepsilon_\Lambda \right), \tag{6}$$

where E_x denotes the internal excitation energy of the residual nucleus, and its recoil energy is taken into account with its mass $M_{A-2} = (A-2)M_N$ being used for simplicity. ε_N and ε_Λ are the binding energies of a nucleon and a Λ in the initial state, respectively.

The expression for $\Gamma_{\rm nm}$ in the shell model basis is given in Eq. (2.9) of Ref. [10] or Eq. (30) of Ref. [25]. $\Gamma_{\rm nm}$ is composed of the proton-stimulated decay rate $\Gamma_p(\Lambda p \to np)$ ($\nu_N = -1/2$ for the proton) and the neutron-stimulated one $\Gamma_n(\Lambda n \to nn)$ ($\nu_N = +1/2$ for the neutron) as

$$\Gamma_{\rm nm} = \Gamma_p + \Gamma_n. \tag{7}$$

If the hypernuclei are polarized at the initial stage, the emitted protons (neutrons) in the non-mesonic decays show asymmetric angular distribution with respect to the plane perpendicular to the polarization axis. This is characteristic to the weak process in which interference between the parity-conserving and parity-violating amplitudes takes place. In the case where the initial hypernuclear states have pure vector polarization $\boldsymbol{P}_H = P_H \boldsymbol{n}$, with $\boldsymbol{n}$ being the polarization direction, the hypernuclear ensemble is expressed in terms of a density matrix $\rho_{\rm pol}$ as [35,36]

$$\rho_{\rm pol} = \frac{1}{2J_H + 1}\left[1 + \frac{3}{J_H + 1}(\boldsymbol{P}_H \cdot \boldsymbol{J}_H)\right], \tag{8}$$

where $\boldsymbol{J}_H$ is the hypernuclear spin.

The angular distribution of decay protons is calculated by fixing the direction $\hat{\boldsymbol{k}}_p$ of the proton as [37]

$$\begin{aligned} \frac{d\Gamma(J_H T_H, P_H \to \hat{\boldsymbol{k}}_p, \nu_p)}{d\Omega_{\hat{\boldsymbol{k}}_p}} &= {\rm Tr}\,(T \rho_{\rm pol} T^\dagger) \\ &= \Gamma_0 + \Gamma_1 P_H \cos\theta_p \\ &= \Gamma_0 (1 + \alpha_1 P_H \cos\theta_p) \end{aligned} \tag{9}$$

with

$$\alpha_1 = \frac{\Gamma_1}{\Gamma_0}. \tag{10}$$

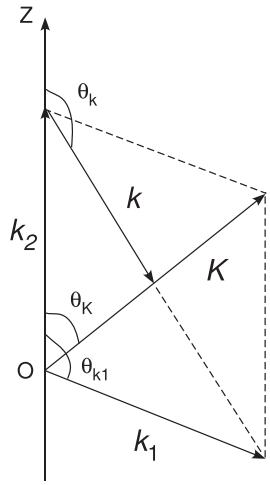

Fig. 1. Momentum vectors of the outgoing neutron $\boldsymbol{k}_1$ and proton $\boldsymbol{k}_2$, and the relative momentum vector $\boldsymbol{k}$ and total momentum vector $\boldsymbol{K}$ of the two outgoing nucleons.

The angle θ_p of the emitted proton is measured from the polarization direction $\boldsymbol{n}$ as defined by $\cos\theta_p = (\boldsymbol{n}\cdot\hat{\boldsymbol{k}}_p)$. α_1 is the asymmetry parameter of the emitted proton angular distribution for the hypernuclear spin J_H. Γ_0 is related to $\Gamma_p(\Lambda p \to np)$ as $\Gamma_0 = \Gamma_p/4\pi$.

Hereafter we use the notation $\boldsymbol{k}_2 = \boldsymbol{k}_p$ for the outgoing proton momentum and $\boldsymbol{k}_1$ for the outgoing neutron one, corresponding to the two-body process of $\Lambda + p \to n + p$. The momentum vectors are depicted in Fig. 1 in the proton helicity frame.

Γ_1 in Eq. (9) is expressed as [10,26]

$$\begin{aligned}\Gamma_1 = {} & \frac{2\pi}{2J_H+1}\frac{3}{J_H+1}\sum_{J'_1M'_1\alpha'_1}\sum_{T'_1M'_{T_1}}\sum_{S'_2M'_{S_2}}\sum_{M_H}\int\frac{d\boldsymbol{k}_1}{(2\pi)^3}\int\frac{k_2^2dk_2}{(2\pi)^3}\,\delta(E_f-E_i)\\ & \times\left|\left\langle\sum_{T'_2}{}^{A-2}\Phi_{J'_1M'_1\alpha'_1,T'_1M'_{T_1}}\,\frac{1}{\sqrt{2}}\left[1-(-1)^{S'_2+T'_2}P_x\right]e^{i\boldsymbol{k}\cdot\boldsymbol{r}}e^{i\boldsymbol{K}\cdot\boldsymbol{R}}\right.\right.\\ & \left.\left.\times\,\chi^{S'_2}_{M'_{S_2}}\xi^{T'_2}_{M'_{T_2}=0}\,|\sum_{ik}V_{\rm nm}(i,k)\,|\,{}^A_\Lambda\Psi\,;J_HM_H,\,T_HM_{T_H}\right\rangle\right|^2\cdot M_H. \end{aligned} \tag{11}$$

In evaluating Γ_1 of Eq. (11), we choose

$$k_2, \quad \theta_{k_1}, \quad \text{and} \quad \phi_{k_1} \tag{12}$$

for the three independent integral variables [38], and the following notations are used:

$$k_Q = \sqrt{2M_N[M_\Lambda - M_N + \epsilon_N + \epsilon_\Lambda - E_x\,(A-2, J'_1T'_1\alpha'_1)]}, \tag{13}$$

$$k_1 = \frac{-k_2\cos\theta_{k_1} + \sqrt{(A-1)(A-2)k_Q^2 - k_2^2[(A-1)^2 - \cos^2\theta_{k_1}]}}{A-1}, \tag{14}$$

$$k_{2,\max} = \sqrt{\frac{A-2}{A-1}}\,k_Q, \tag{15}$$

$$4k^2 = k_1^2 + k_2^2 - 2k_1k_2\cos\theta_{k_1}, \tag{16}$$

$$K^2 = k_1^2 + k_2^2 + 2k_1k_2\cos\theta_{k_1}, \tag{17}$$

$$\phi_k = \phi_K, \tag{18}$$

$$\cos\theta_k = \frac{1}{2k}(-k_2 + k_1\cos\theta_{k_1}), \tag{19}$$

$$\cos\theta_K = \frac{1}{K}(k_2 + k_1\cos\theta_{k_1}). \tag{20}$$

When the shell model wave functions are adopted for the initial hypernuclear and final nuclear states, and when the weak decays take place from the Λ-proton (nucleon) relative S-state, the detailed expression of Γ_1 is obtained as given in Appendix A. In Eq. (A.1), the Block–Dalitz notations [39] for the $\Lambda p \to np$ transition amplitudes, a, b, c, d, e, and f, are introduced conventionally, which express the possible non-mesonic decay channel transitions, respectively. Also, for convenience of later discussions, we give here the "channel numbers" Ch.1–6 to these channels as follows:

$$\begin{aligned}&\text{Ch.1}: a(^1S_0 \to {}^1S_0), \quad \text{Ch.2}: b(^1S_0 \to {}^3P_0), \quad \text{Ch.3}: c(^3S_1 \to {}^3S_1),\\ &\text{Ch.4}: d(^3S_1 \to {}^3D_1), \quad \text{Ch.5}: e(^3S_1 \to {}^1P_1), \quad \text{Ch.6}: f(^3S_1 \to {}^3P_1).\end{aligned} \tag{21}$$

The two-body amplitudes are defined as

$$\left\langle i^{\ell_0} j_{\ell_0}(k,r)\mathcal{Y}_{\ell_0 S_2' \mathcal{J}}\xi^{T_2'}_{M_{T_2'}=0} \,|\, V_{\rm nm}(\boldsymbol{r}) \,|\, \phi_{n\ell=0}(r,b_r)\mathcal{Y}_{\ell=0 S \mathcal{J}=S}\xi^{T_2=1/2}_{\nu_p=-1/2}\right\rangle. \tag{22}$$

As mentioned above, the asymmetry parameter α_1 of the emitted protons in Eq. (10) is defined for the polarized hypernuclei with spin J_H and polarization P_H. However, one often discusses the Λ-polarization P_Λ and the asymmetry parameter α_Λ for the polarized Λ hyperon in the nuclear medium. For comparison we note the following relations when the hypernuclear state is well described in the weak coupling model of Λ in the $s^\Lambda_{1/2}$ state and the core-nucleus state of J_c. The asymmetry is written as

$$\mathcal{A} = P_H\alpha_1 = P_\Lambda\alpha_\Lambda, \tag{23}$$

and the relation holds well in the weak coupling model as

$$\begin{aligned}P_\Lambda &= -\frac{J_H}{J_H+1}P_H \quad \text{if} \quad J_H = J_c - 1/2,\\ &= P_H \quad \text{if} \quad J_H = J_c + 1/2.\end{aligned} \tag{24}$$

Then it follows from Eq. (23) that

$$\begin{aligned}\alpha_\Lambda &= -\frac{J_H+1}{J_H}\alpha_1 \quad \text{if} \quad J_H = J_c - 1/2,\\ &= \alpha_1 \quad \text{if} \quad J_H = J_c + 1/2.\end{aligned} \tag{25}$$

The quantity α_Λ is referred to as the intrinsic asymmetry parameter for the polarized Λ hyperon in the hypernucleus having spin J_H. The intrinsic α_Λ should be compared to the asymmetry parameter $\alpha_\Lambda^{\rm elem}$ for the elementary process $\vec{\Lambda} + p \to n + p$ in free space, when the Λ hyperon is polarized. We quote here $\alpha_\Lambda^{\rm elem}$ in terms of Block–Dalitz amplitudes $\{a, b, \ldots, f\}$ when the initial Λ-proton is assumed to be in a relative S-state [10]:

$$\alpha_\Lambda^{\rm elem} = \frac{2\sqrt{3}\,{\rm Re}\,[\,-ae^* + b(c-\sqrt{2}d)^*/\sqrt{3} + f(\sqrt{2}c+d)^*\,]}{|a|^2+|b|^2+3\,[|c|^2+|d|^2+|e|^2+|f|^2\,]}. \tag{26}$$

3. Meson exchange model to construct $\Lambda N \to NN$ weak decay potentials

The weak decay potentials for the transition $\Lambda N \to NN$ ($\Delta S = 1$) are constructed in the meson exchange model. The following guiding principles are adopted in devising the potentials.

(1) Meson exchanges are considered as completely in quantum numbers as possible. For those mesons we include:
  (i) pseudoscalar (ps) ($J^{\rm PC} = 0^{-+}$): π, K
  (ii) vector (vec) ($J^{\rm PC} = 1^{--}$): ρ, K^*, ω
  (iii) scalar (sc) ($J^{\rm PC} = 0^{++}$): σ, κ
  (iv) axial-vector (avec) ($J^{\rm PC} = 1^{++}$, first kind): a_1, K_1.
(2) Non-strange mesons and strange mesons are considered on an equal footing.
(3) Pomeron (pom) ($J^{\rm PC} = 0^{++}$) P exchange is included.
(4) For the coupling constants of the baryon–baryon–meson strong vertices we adopt those of the Nijmegen ESC08c model in the recent 2016 version [32,33].
(5) For the coupling constants of the baryon–baryon–meson weak vertices we accept the empirical values of $\Lambda N\pi$ and $\Sigma N\pi$ weak vertices, and also, for the other vertices, the theoretical ones from the work of Parreño et al. in Ref. [21].
(6) When the meson–meson–meson coupling constants are needed in constructing our model, we use the empirical value if it is known or we determine them by imposing the constraints on our potential model as described later.
(7) The $\Delta I = 1/2$ rule is assumed for the weak baryon–baryon–meson coupling Hamiltonians.

Correspondingly, here we extend our basic framework [10,26] to include new processes of meson exchanges such as K^*, κ, and K_1, and the pomeron exchange as well. Two types of meson exchange potentials between Λ and N are introduced. The first type is the ordinary one-meson exchange potentials such as V_π, V_K, V_{K^*}, and V_ω, corresponding to π, K, K^*, and ω exchange, respectively. The second one (we call this Y-type) is the correlated two-meson/meson exchange potentials in which the two mesons are correlated and coupled to one meson with specified quantum numbers in the intermediate state. In other words, one meson is dissociated into two mesons in the intermediate state during the interaction process between Λ and N. In this way the ρ, σ, κ, a_1, and K_1 meson exchanges can be treated systematically, and these Y-type processes are called in our paper as exchanges of $2\pi/\rho$, $2\pi/\sigma$, $K\pi/\kappa$, $(\rho\pi/a_1, \sigma\pi/a_1)$, and $K^*\pi/K_1$, respectively. Thus we designate $V_{2\pi/\rho}$, $V_{2\pi/\sigma}$, $V_{K\pi/\kappa}$, $(V_{\rho\pi/a_1}, V_{\sigma\pi/a_1})$, and $V_{K^*\pi/K_1}$ as these meson exchange potentials. The pomeron exchange is treated similarly as the $2\pi/P$ exchange, and the potential is denoted as $V_{2\pi/P}$.

We briefly comment here on the pomeron coupling to mesons and baryons. Besides meson exchange, pomeron exchange is needed to understand the high energy dependence ($\sqrt{s}$) of all hadronic cross sections such as $\pi^\pm p, pN, \bar{p}N$, etc. A low-energy extrapolation of pomeron exchange in πN and NN scattering leading to the pomeron–nucleon and pomeron–pion coupling has been used in the Nijmegen soft-core models [31,40]. This is also applied in this paper. From the point of view of chiral symmetry in πN scattering, the cancellation between sigma and pomeron exchange is important in order to have a small $I = 0$ scattering length. Therefore, next to $2\pi/\sigma$, $2\pi/P$ exchange weak decay graphs are also included in our work.

As a typical example, the $K\pi/\kappa$ exchange consists of four kinds of Y-type Feynman diagrams as shown in Fig. 2(a1), (a2), (b), and (c). They are distinguished by an intermediate baryon, a nucleon, Λ, and Σ, respectively. The contributions of the diagrams (a1)+(a2), (b), and (c) to the potentials are

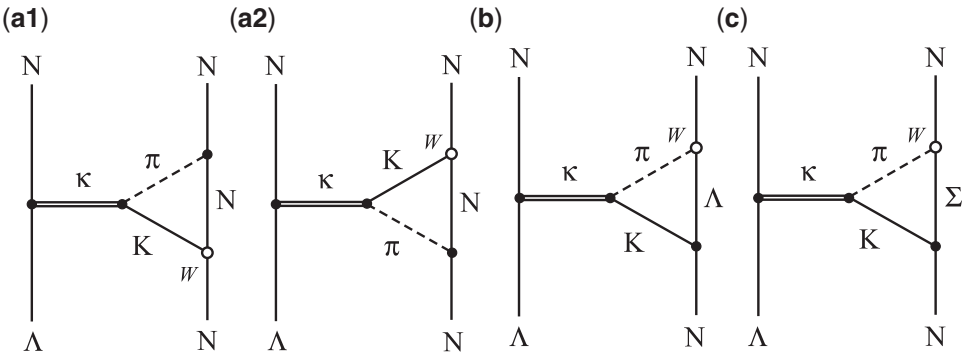

Fig. 2. Y-type Feynman diagrams of $\Lambda N \to NN$ for $K\pi/\kappa$ exchange. The diagrams (a1) and (a2) contain a N in the intermediate baryon line, while (b) and (c) contain Λ and Σ instead. The weak vertices are marked by an open circle.

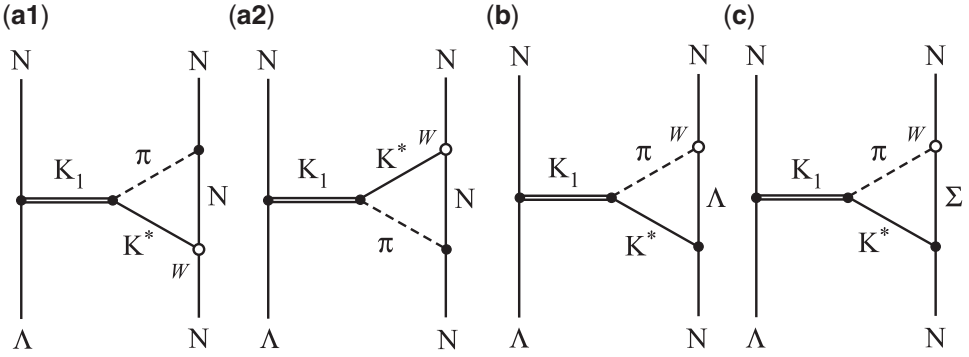

Fig. 3. Y-type Feynman diagrams of $\Lambda N \to NN$ for $K^*\pi/K_1$ exchange. See also the caption to Fig. 2.

termed $V_{K\pi/\kappa(A)}$, $V_{K\pi/\kappa(B)}$, and $V_{K\pi/\kappa(C)}$. The potential $V_{K\pi/\kappa}$ represents

$$V_{K\pi/\kappa} = V_{K\pi/\kappa(A)} + V_{K\pi/\kappa(B)} + V_{K\pi/\kappa(C)}. \tag{27}$$

In Fig. 3 we show the Feynman diagrams of $K^*\pi/K_1$ exchange. Corresponding to the diagrams (a1)+(a2), (b), and (c) in Fig. 3, the potentials of $V_{K^*\pi/K_1(A)}$, $V_{K^*\pi/K_1(B)}$, $V_{K^*\pi/K_1(C)}$ are calculated, respectively. The potential $V_{K^*\pi/K_1}$ represents

$$V_{K^*\pi/K_1} = V_{K^*\pi/K_1(A)} + V_{K^*\pi/K_1(B)} + V_{K^*\pi/K_1(C)}. \tag{28}$$

For the correlated two-meson/meson exchange potentials, the loop integrals have to be performed for the loop momentum. One faces three kinds of loop integrals:

(1) For scalar meson exchanges such as $2\pi/\sigma$ and $K\pi/\kappa$, and also for the $2\pi/P$ exchange, the loop integrals do not diverge.
(2) For a vector meson exchange such as $2\pi/\rho$ and for the axial-vector meson exchange of $\sigma\pi/a_1$, the loop integrals diverge since the integrands have forms like

$$G(k) = \frac{F_0 + F_1 k^2}{[k^2 - c]^3}, \tag{29}$$

where k is a loop momentum. For the first the k_0-integration is performed and the three-dimensional $\boldsymbol{k}$-integration is left. In order to circumvent the divergence, we introduce a form

factor of the form

$$\frac{\Lambda_1^2}{\boldsymbol{k}^{\,2}+\Lambda_1^2}, \tag{30}$$

where $\boldsymbol{k}$ is the three-momentum and Λ_1 is the cutoff mass parameter.

(1) For axial-vector meson exchanges such as $\rho\pi/a_1$ and $K^*\pi/K_1$, the loop integrals contain integrands like

$$G(k) = \frac{F_0 + F_1 k^2 + F_2 k^4}{[k^2 - c]^3}, \tag{31}$$

and the integrals diverge. Similarly to the preceding case, the k_0-integration is carried out first. Then, in order to regularize the $\boldsymbol{k}$ -integral, we introduce a form factor of the form

$$\left[\frac{\Lambda_2^2}{\boldsymbol{k}^{\,2}+\Lambda_2^2}\right]^2, \tag{32}$$

where $\boldsymbol{k}$ is the three-momentum and Λ_2 is the cutoff mass parameter.

We use the vertex form factor (FF) to obtain the potentials. For the one-π exchange, we use a global FF of the monopole type as described in Ref. [25]. For other one-meson exchange potentials, double FFs such as $\left[\frac{\Lambda_i^2}{\boldsymbol{q}^{\,2}+\Lambda_i^2}\right]^2$ are adopted, where $\boldsymbol{q}$ is the momentum transfer and Λ_i is the cutoff mass for the exchanged meson i. For the case of the correlated two-meson/meson exchange potentials like $2\pi/\rho$, $\rho\pi/a_1$, $\sigma\pi/a_1$, and $K^*\pi/K_1$, we use the single-vertex FF $\left[\frac{\Lambda_i^2}{\boldsymbol{q}^{\,2}+\Lambda_i^2}\right]$ for the baryon–baryon–meson strong vertex [N–N–meson (non-strange) or Λ–N–meson (strange)] part. This is because the correlated two-meson/meson exchange potentials involve the loop integral and contain the regularization FF, and such parts are supposed to act like a sort of vertex form factor. For the scalar meson exchanges such as $2\pi/\sigma$ and $K\pi/\kappa$, the "zero" form factor is considered [10,26,41] and the vertex FF takes the form $(1-\frac{\boldsymbol{q}^2}{U_x^2})\frac{\Lambda_i^2}{\boldsymbol{q}^{\,2}+\Lambda_i^2}$, where U_x is a mass parameter.

The actual types of the weak potentials depend on the exchanged mesons [10,25,26]. We show here the $K^*\pi/K_1$ exchange potentials that correspond to the (a1)+(a2), (b), and (c) diagrams in Fig. 3:

$$\begin{aligned} V_{K^*\pi/K_1(A)} = {} & \big\{V_S(r)(\boldsymbol{\sigma}_1\cdot\boldsymbol{\sigma}_2) + V_T(r)S_{12} + V_{LS}(r)(\boldsymbol{L}\cdot\boldsymbol{S}) \\ & + i\,V_{V_1}(r)\,i[(\boldsymbol{\sigma}_1\times\boldsymbol{\sigma}_2)\cdot\hat{\boldsymbol{r}}] + i\,V_{V_2}(r)\,(\boldsymbol{\sigma}_2\cdot\hat{\boldsymbol{r}})\big\}\,(\boldsymbol{\tau}_1\cdot\boldsymbol{\tau}_2), \end{aligned} \tag{33}$$

$$V_{K^*\pi/K_1(B)} = \big\{\text{ same potential type as in Eq. (33) }\big\}\cdot\left(\frac{3}{2} - \frac{1}{2}(\boldsymbol{\tau}_1\cdot\boldsymbol{\tau}_2)\right), \tag{34}$$

$$\begin{aligned} V_{K^*\pi/K_1(C)} = {} & \big\{V_S(r)(\boldsymbol{\sigma}_1\cdot\boldsymbol{\sigma}_2) + V_T(r)S_{12} + V_{LS}(r)(\boldsymbol{L}\cdot\boldsymbol{S})\big\}\cdot(\,a_0 + a_1(\boldsymbol{\tau}_1\cdot\boldsymbol{\tau}_2)\,) \\ & + \big\{i\,V_{V_1}(r)\,i[(\boldsymbol{\sigma}_1\times\boldsymbol{\sigma}_2)\cdot\hat{\boldsymbol{r}}] + i\,V_{V_2}(r)\,(\boldsymbol{\sigma}_2\cdot\hat{\boldsymbol{r}})\big\}\cdot(\,b_0 + b_1(\boldsymbol{\tau}_1\cdot\boldsymbol{\tau}_2)\,), \end{aligned} \tag{35}$$

where a_0, a_1, b_0, and b_1 are expressed in terms of the weak coupling constants of $\Sigma \to N + \pi$ decays. Particle 1 refers to a Λ hyperon. The parity-violating potentials are expressed as imaginary. It is noted that the K_1 exchange potentials have no simple isospin dependence except for $V_{K^*pi/K_1(A)}$, i.e. the potentials have factors with a mixture of isoscalar and $(\boldsymbol{\tau}_1\cdot\boldsymbol{\tau}_2)$ dependence. This is because the K_1 meson is an iso-doublet particle.

4. Initial and final wave functions and calculated non-mesonic weak decay potentials

4.1. Initial hypernuclear states and final nuclear states

The hypernuclear ground state is well represented in the weak-coupling model of the nuclear shell model lowest state coupled with a Λ hyperon in the s-state. For the Λ hyperon state we use a solution of the density-dependent Hartree–Fock equation of the core-nucleus+Λ system. The Λ wave function is expanded in the harmonic oscillator basis for further manipulation. The details are given in Refs. [10,25].

In evaluating the $\Lambda N \to NN$ transition matrix element, we take into account the initial ΛN-state correlation (called ISC) and the final NN-state correlation (FSC) properly. The ISC in the nuclear medium is treated by solving the Bethe–Goldstone equation for the ΛN relative S-state with the use of Nijmegen model-D interaction [42,43]. Then the initial state $\phi_{n\ell=0}(r, b_r)\mathcal{Y}_{\ell=0S\mathcal{J}}$ in Eq. (22) is replaced as

$$\phi_{n0}(r, b_r)\mathcal{Y}_{0SS} \longrightarrow f_S(r)\phi_{n0}(r, b_r)\mathcal{Y}_{0SS} + \delta_{S,1} f_2(r)\mathcal{Y}_{211} \tag{36}$$

for the $S(\ell = 0)$ wave. $f_S(r)$ is the correlation function for the S wave of spin $\mathcal{S}$-state, and $f_2(r)$ is the induced $D(\ell = 2)$ wave for the initial ${}^3S_1$ state.

For the final outgoing two-nucleon states, the scattering states are solved by the Runge–Kutta method. For the NN ${}^3S_1$ and ${}^3D_1$ states in particular, the coupled channel equations due to the tensor interaction are solved. We use the Nijmegen model-D for the NN strong interaction [42,43]. Thus the partial wave $i^{\ell_0} j_{\ell_0}(k, r)\mathcal{Y}_{\ell_0 S_2' \mathcal{J}}$ in Eq. (22) is replaced as

$$\begin{aligned} i^{\ell_0} j_{\ell_0}(k, r)\mathcal{Y}_{\ell_0 S_2' \mathcal{J}} \longrightarrow\ & i^{\ell_0}\, \psi_{\ell_0 S_2' \mathcal{J}}(k, r)\mathcal{Y}_{\ell_0 S_2' \mathcal{J}} \\ & + \delta_{S_2',1}\delta_{\mathcal{J},1}\left[\, \delta_{\ell_0,0} i^2 \chi_2(k, r)\mathcal{Y}_{211} + \delta_{\ell_0,2} i^0 \chi_0(k, r)\mathcal{Y}_{011}\,\right]. \end{aligned} \tag{37}$$

The function $\psi_{\ell_0 \mathcal{S}_2' \mathcal{J}}(k, r)$ denotes the scattering wave. The functions $\chi_2(k, r)$ and $\chi_0(k, r)$ are the induced D wave for the final ${}^3S_1$ state and the induced S wave for the final ${}^3D_1$ state, respectively, due to the tensor interaction. The coupled-channel solutions for the final two-nucleon relative wave functions for ${}^3S_1$ and ${}^3D_1$, and their induced waves $i^2\chi_2$ and $i^0\chi_0$, are shown for a typical momentum case ($k = 370.0$ MeV/c) in Fig. 7 of Bandō's paper [1].

4.2. Behaviors obtained for weak decay transition potentials

The $\Lambda N \to NN$ weak decay potentials are calculated based on the Feynman diagrams. It is characteristic that the strangeness-changing $\Lambda N \to NN$ weak interaction allows both exchanges of non-strange mesons and strange mesons between Λ and N. The adopted strong coupling constants of baryon–baryon–meson (BBM) and meson–meson–meson (MMM) vertices are summarized in Table 1, which also lists meson masses, cutoff masses in the vertex form factors, and cutoff mass parameters in the regularization form factors. Table 2 presents the weak coupling constants of baryon–baryon–meson vertices.

The BBM strong coupling constants are those determined in the 2016 version of the Nijmegen ESC08c model [32,33], and the weak coupling constants of NNK, NNK^*, and $\Lambda N\omega$ are taken from Ref. [21]. The cutoff mass Λ_i in the vertex FF for the K, K^*, and ω exchange are taken from papers of Ueda et al. [44,45], while the other Λ_i are determined so that our FF simulates the Nijmegen FF

Table 1. Strong coupling constants of baryon–baryon–meson and meson–meson–meson vertices, cutoff masses in the baryon–baryon–meson vertex FF, and cutoff mass parameters in the regularization FF employed in our potentials. The meson masses, cutoff masses, and cutoff mass parameters are given in MeV. The coupling constants marked with a * have signs opposite to the conventional ones due to the definition of our relevant Hamiltonians (see Appendix B).

		Strong coupling constants		
Meson	Mass	BBM	MMM	Cutoff mass
π	139.57	$g_{NN\pi} = 12.807$		$\Lambda_\pi = 920.0$
		$g_{\Lambda\Sigma\pi} = 9.391$		
K	493.67	$g_{\Lambda NK} = -14.002$		$\Lambda_K = 1129.5$
		$g_{\Sigma NK} = 3.925$		
ρ	771.10	$g_{NN\rho} = 2.248$	$g_{\pi\pi\rho} = -5.90$*	$\Lambda_\rho = 800.0$
		$f_{NN\rho} = 13.579$		$\Lambda_1(2\pi/\rho) = 750.0$
		$g_{\Lambda\Sigma\rho} = 0.0$		
		$f_{\Lambda\Sigma\rho} = 8.271$		
K^*	891.66	$g_{\Lambda NK^*} = -3.894$		$\Lambda_{K^*} = 1129.5$
		$f_{\Lambda NK^*} = -15.249$		
		$g_{\Sigma NK^*} = -2.249$		
		$f_{\Sigma NK^*} = 0.747$		
ω	782.80	$g_{NN\omega} = 11.943$		$\Lambda_\omega = 1129.5$
		$f_{NN\omega} = -2.723$		
σ	600.00	$g_{NN\sigma} = 6.30$	$g_{\pi\pi\sigma} = -1850.0$ MeV*	$\Lambda_\sigma = 1130.0$
				$U_x = 750.0$
κ	800.00	$g_{\Lambda N\kappa} = -3.900$	$g_{K\pi\kappa} = -2340.0$ MeV*	$\Lambda_\kappa = 900.0$
				$U_x = 750.0$
a_1	1230.00	$g_{NNa_1} = -2.896$*	$g_{\rho\pi a_1} = -1660.0$ MeV*	$\Lambda_{a_1} = 1380.0$
		$f_{NNa_1} = 9.163$*	$g_{\sigma\pi a_1} = 5.791$	$\Lambda_2(\rho\pi/a_1) = 900.0$
				$\Lambda_1(\sigma\pi/a_1) = 750.0$
K_1	1403.00	$g_{\Lambda NK_1} = -2.774$*	$g_{K^*\pi K_1} = -3835.0$ MeV*	$\Lambda_{K_1} = 1380.0$
		$f_{\Lambda NK_1} = 8.778$*		$\Lambda_2(K^*\pi/K_1) = 900.0$
P	223.12	$g_{NNP} = 11.793$	$g_{\pi\pi P} = -4280.0$ MeV*	

[32,33] approximately,

$$\left[\frac{\Lambda_i^2}{\boldsymbol{q}^2+\Lambda_i^2}\right]^2 \approx \exp\left(-\frac{\boldsymbol{q}^2}{\Lambda_i^2(\mathrm{ESC})}\right), \tag{38}$$

for $q = 400$–800 MeV/c, which is effective in the non-mesonic weak decay process. We take the value $U_x = 750$ MeV from Refs. [32,33]. The MMM coupling constants are determined as described below. The empirical value is adopted for $g_{\pi\pi\rho}$ [46], while $g_{\pi\pi\sigma}$ is the same as in Refs. [10,26]. The coupling constant $g_{\sigma\pi a_1}$ is determined by the relation $g_{\sigma\pi a_1} = 2g_{NNa_1}$, which comes if we consider an almost conserved axial current [26,41]. The coupling constant $g_{\rho\pi a_1}$ and the cutoff mass parameter $\Lambda_2(\rho\pi/a_1)$ for the $\rho\pi/a_1$-exchange potential are determined as follows. We construct the strong NN potential version in the $\rho\pi/a_1$-exchange model by replacing Λ by N and replacing the weak $\Lambda N\pi$ vertex by the strong $NN\pi$ one in the weak potential model. Then $g_{\rho\pi a_1}$ and $\Lambda_2(\rho\pi/a_1)$ are determined so that our potential $V^{\mathrm{strong}}_{\rho\pi/a_1}(NN\text{–}NN)$ can simulate the strong potential $V^{\mathrm{strong}}_{a_1}(NN\text{–}NN)$ in the ESC08c model as well as possible,

$$V^{\mathrm{strong}}_{\rho\pi/a_1}(NN\text{–}NN) \approx V^{\mathrm{strong}}_{a_1}(NN\text{–}NN). \tag{39}$$

Table 2. Parity-conserving (PC) and parity-violating (PV) weak coupling constants. The weak coupling constants for the π decays of Λ and Σ hyperons are given in units of 10^{-6}, while those for other mesons are given in units of $G_F m_\pi^2 = 2.21 \times 10^{-7}$. The weak coupling constants for NNK, NNK^*, and $\Lambda N\omega$ vertices are adopted from Ref. [21]. The masses are given in MeV.

		Weak coupling constants	
Meson	Mass	PC	PV
π	139.57	$\lambda_\Lambda g^w_{\Lambda N\pi} = -1.727$	$g^w_{\Lambda N\pi} = 0.233$
		$\lambda_{\Sigma^+_+} g^w_{\Sigma^+_+} = -4.384$	$g^w_{\Sigma^+_+} = 0.013$
		$\lambda_{\Sigma^0_0} g^w_{\Sigma^0_0} = -2.031$	$g^w_{\Sigma^0_0} = 0.220$
		$\lambda_{\Sigma^-_-} g^w_{\Sigma^-_-} = 0.159$	$g^w_{\Sigma^-_-} = 0.426$
K	493.67	$C_K^{\rm PC} = -18.9$	$C_K^{\rm PV} = 0.76$
		$D_K^{\rm PC} = 6.63$	$D_K^{\rm PV} = 2.09$
K^*	891.66	$C_{K^*}^{{\rm PC},V} = -3.61$	$C_{K^*}^{\rm PV} = -4.48$
		$C_{K^*}^{{\rm PC},T} = -17.9$	
		$D_{K^*}^{{\rm PC},V} = -4.89$	$D_{K^*}^{\rm PV} = 0.60$
		$D_{K^*}^{{\rm PC},T} = 9.30$	
ω	782.80	$\alpha_\omega = -3.69$	$\epsilon_\omega = -1.33$
		$\beta_\omega = -8.04$	

The values $g_{K^*\pi K_1}$ and $\Lambda_2(K^*\pi/K_1)$ are determined in a similar manner to the case of $g_{\rho\pi a_1}$ and $\Lambda_2(\rho\pi/a_1)$. We take $\Lambda_2(K^*\pi/K_1) = \Lambda_2(\rho\pi/a_1)$ for simplicity. The cutoff mass parameter $\Lambda_1(2\pi/\rho)$ is determined so as to fulfill the relation

$$V^{\rm strong}_{2\pi/\rho}(NN\text{–}NN) \approx V^{\rm strong}_{\rho}(NN\text{–}NN), \tag{40}$$

where the right-hand side is the potential in the ESC08c model. The pomeron coupling constant $g_{\pi\pi P}$ is treated as an adjustable parameter so that the calculated non-mesonic decay rates and asymmetry parameter of ${}^{5}_{\Lambda}$He reproduce the available data, in which particularly the experimental errors for α_Λ are small enough to be used as a good restriction on the theory. As a matter of course, we have paid attention to whether the strong $V^{\rm strong}_{2\pi/P}(NN\text{–}NN)$ properly simulates the $V^{\rm strong}_{P}(NN\text{–}NN)$ in the ESC08c model.

The calculated meson exchange potentials are displayed in Figs. 4–9 for the six decay channels to which the transition amplitudes $\{a, b, c, d, e, f\}$ correspond, and we give them the channel numbers Ch.1–Ch.6, respectively, as defined by Eq. (21). Three panels, (a), (b), and (c), are shown in Figs. 4–8, while only two panels, (a) and (b), are shown in Fig. 9. Consider, for instance, Fig. 4 for the $({}^1S_0)_{\Lambda p} \to ({}^1S_0)_{np}$ channel. The panel (a) plots two lines of potentials: one is the potential V(Sum1) coming from the partial summation over the "pseudoscalar + vector" meson exchanges, and the other is the total potential V(SUM) including all mesons and pomeron exchange: SUM = Sum1 + "scalar + axial-vector" meson exchanges + pomeron exchange. For easy understanding we denote them as follows:

$$V(\text{Sum1}) = V_\pi + V_K + V_{2\pi/\rho} + V_{K^*} + V_\omega, \tag{41}$$

$$V(\text{SUM}) = V_\pi + V_K + V_{2\pi/\rho} + V_{K^*} + V_\omega + V_{2\pi/\sigma} + V_{K\pi/\kappa} + V_{2\pi/P} + V_{\rho\pi/a_1} + V_{\sigma\pi/a_1} + V_{K^*\pi/K_1}. \tag{42}$$

A note is added for special channels. In Fig. 7(a) of the $(^3S_1)_{\Lambda p} \to (^3D_1)_{np}$ channel, V(SUM) does not include contributions from $V_{2\pi/\sigma}$, $V_{K\pi/\kappa}$, and $V_{2\pi/P}$, and in Fig. 9(a) of the $(^3S_1)_{\Lambda p} \to (^3P_1)_{np}$ channel, both V(Sum1) and V(SUM) do not include contributions from V_{K^*} and V_ω. In each panel (b) of Figs. 4–8 we show the divided potentials for the pseudoscalar and vector meson exchanges. Panel (c) shows the divided potentials for the scalar and axial-vector meson exchanges and the pomeron exchange. It is noted that in Fig. 7(c) for the tensor interaction channel of $(^3S_1)_{\Lambda p} \to (^3D_1)_{np}$ there is no contribution from the scalar meson and pomeron exchanges. In Fig. 9, panel (b) shows the divided contributions of the pseudoscalar and scalar meson exchanges and the pomeron exchange. Potentials of vector meson (K^*, ω) exchanges do not contribute to this channel. Potentials of other correlated two-meson/meson exchanges of vector and axial-vector mesons are not shown, because they are very small.

4.3. Potential properties based on exchanges of pseudoscalar and vector mesons

The characteristic features found in the calculated potentials are summarized as follows. The parity-conserving (PC) central interaction potentials are shown in Fig. 4(b) for the $(^1S_0)_{\Lambda p} \to (^1S_0)_{np}$ channel—we call this Ch.1, cf. Eq. (21)—and in Fig. 6(b) for $(^3S_1)_{\Lambda p} \to (^3S_1)_{np}$ channel (Ch.3). The potential V_π shows remarkable behavior, almost completely opposite in sign to that of the potential V_K, and these two potentials tend to cancel out in both channels, Ch.1 and Ch.3. Similarly, the $V_{2\pi/\rho}$ potential also has notable behavior opposite in sign to that of the V_{K^*} potential in Ch.1 and Ch.3, though, particularly in Ch.3, $V_{2\pi/\rho}$ is strong and positive at $R \gtrsim 0.5$ fm while V_{K^*} is weak and negative at $R \gtrsim 0.6$ fm. These features show the role of the non-strange meson (π, ρ) and strange meson (K, K^*) exchanges. The V_ω potential is strong and negative. As a result, the potentials V(Sum1) in Ch.1 and Ch.3 turn out to be negative, as seen in Figs. 4(a) and 6(a). The PC tensor interaction potentials are shown in Fig. 7(b) for $(^3S_1)_{\Lambda p} \to (^3D_1)_{np}$ channel (Ch.4). The potential V_π shows the characteristic behavior opposite in sign to the potential V_K, though V_π is rather stronger in strength than V_K at all interaction ranges. V_π is positive. Likewise, the two potentials $V_{2\pi/\rho}$ and V_{K^*} show opposite behaviors, different in sign from each other, though V_{K^*} is a little stronger than $V_{2\pi/\rho}$. V_{K^*} is positive. Also, in the tensor interaction channel (Ch.4), one notices the clearly different contributions to the potentials from the non-strange meson (π, ρ) and the strange meson (K, K^*) exchanges. The V_ω potential is weak and positive. As a result, the potential V(Sum1) in Ch.4 turns out to be positive, as seen in Fig. 7(a).

The parity-violating (PV) potentials are shown in Fig. 5(b) for the $(^1S_0)_{\Lambda p} \to (^3P_0)_{np}$ channel (Ch.2), Fig. 8(b) for the $(^3S_1)_{\Lambda p} \to (^1P_1)_{np}$ channel (Ch.5), and Fig. 9(b) for the $(^3S_1)_{\Lambda p} \to (^3P_1)_{np}$ channel (Ch.6). In Ch.2 the two potentials V_π and V_K show opposite behavior in sign, while $V_{2\pi/\rho}$ and V_{K^*} show the same sign behavior. The V_ω potential is weak and positive. Then, the summed potential V(Sum1) in Ch.2 becomes negative due to the strong and negative sign behaviors of V_K and V_{K^*}. The Ch.5 pseudoscalar and vector meson exchange potentials in Fig. 8(b) are interesting. All the potentials contribute in the same positive sign and thus work additively. Among them, the contributions of V_π, V_{K^*}, and $V_{2\pi/\rho}$ are important. Accordingly, the V(Sum1) potential is strong and positive, as seen in Fig. 8(a). Ch.6 for the $(^3S_1)_{\Lambda p} \to (^3P_1)_{np}$ transition is special. The one vector meson exchange potentials such as V_{K^*} and V_ω do not contribute to this channel due to the kinematics for the matrix element on the $i[(\boldsymbol{\sigma}_1 \times \boldsymbol{\sigma}_2) \cdot \hat{\boldsymbol{r}}]$ operator. The pseudoscalar meson exchanges have major contributions. The potentials V_π and V_K work additively in negative sign. Although the $V_{2\pi/\rho}$ potential has a $(\boldsymbol{\sigma}_1 \cdot \hat{\boldsymbol{r}})$-type potential in addition to the $i[(\boldsymbol{\sigma}_1 \times \boldsymbol{\sigma}_2) \cdot \hat{\boldsymbol{r}}]$-type one [25], its contribution is very small and is not shown in Fig. 9(b).

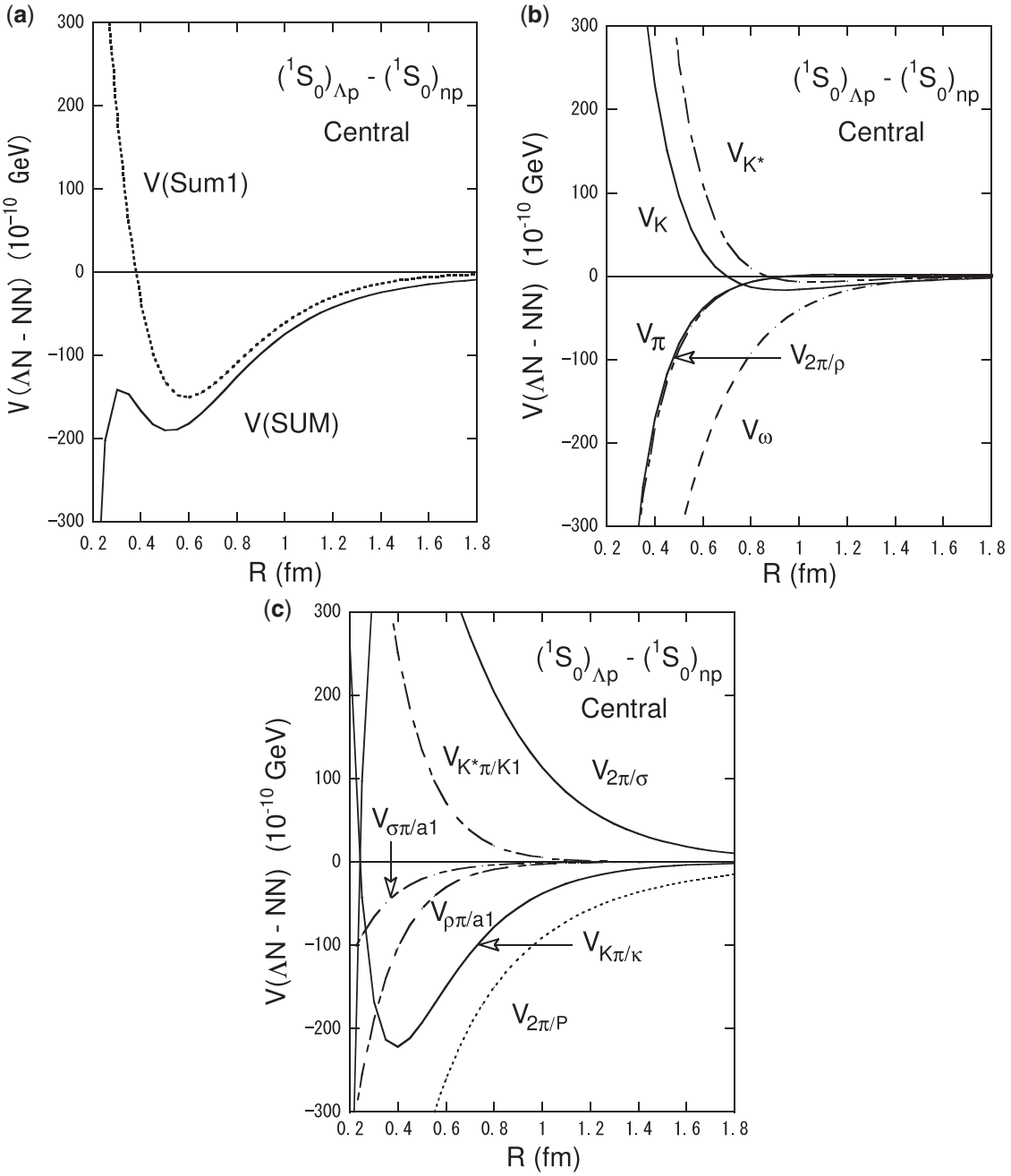

Fig. 4. (Channel 1 (Ch.1)) The central-type weak decay transition potentials for the $(^1S_0)_{\Lambda p} \to (^1S_0)_{np}$ channel. (a) V(Sum1) is the summed potential based on the $(\pi + K + 2\pi/\rho + K^* + \omega)$ meson exchanges, while V(SUM) is the total potential by summing, in addition to V(Sum1), all contributions from the other $(2\pi/\sigma + K\pi/\kappa + \rho\pi/a_1 + \sigma\pi/a_1 + K^*\pi/K_1)$ meson exchanges and the pomeron exchange $(2\pi/P)$. (b) The transition potentials coming from the pseudoscalar mesons $(\pi + K)$ and the vector mesons $(2\pi/\rho + K^* + \omega)$. (c) The transition potentials coming from the scalar mesons $(2\pi/\sigma + K\pi/\kappa)$, the axial-vector mesons $(\rho\pi/a_1 + \sigma\pi/a_1 + K^*\pi/K_1)$, and the pomeron $2\pi/P$ exchange.

4.4. Potential properties based on exchanges of scalar and axial-vector mesons and pomeron

In Ch.1 of Fig. 4(c), the central potentials of $V_{2\pi/\sigma}$ and $V_{2\pi/P}$ work oppositely in sign. This might be interpreted that the effective scalar–isoscalar "σ" meson exchange potential should become weak

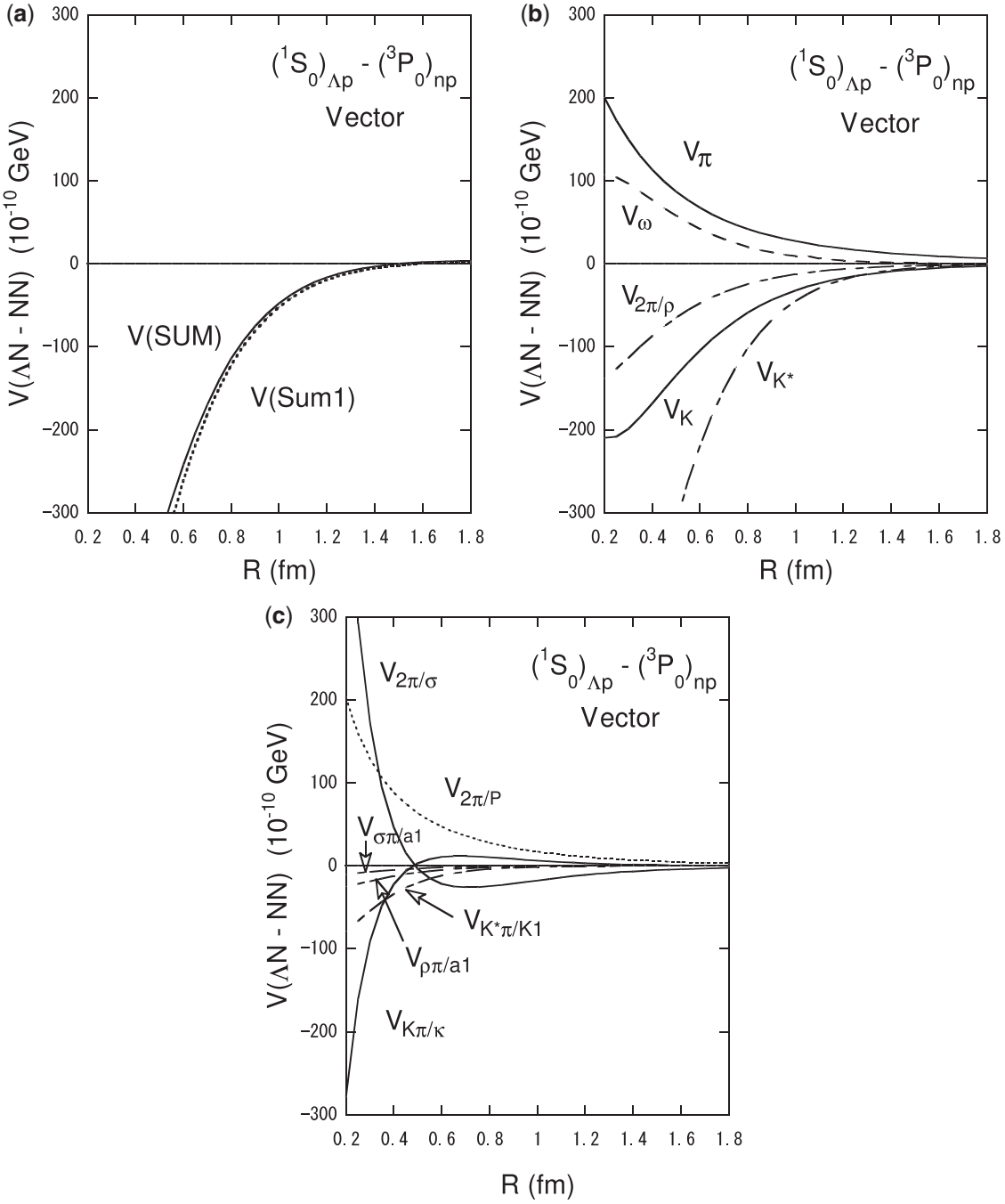

Fig. 5. (Ch.2) The parity-violating vector-type weak decay transition potentials for the $(^1S_0)_{\Lambda p} \to (^3P_0)_{np}$ channel. Panels (a), (b), and (c) are the same as in Fig. 4.

when one considers only the "σ" meson exchange with no pomeron exchange. We notice that the two potentials $V_{2\pi/\sigma}$ and $V_{K\pi/\kappa}$, having opposite signs, tend to diminish each other, and the $V_{\rho\pi/a_1} + V_{\sigma\pi/a_1}$ and $V_{K^*\pi/K_1}$ potentials also behave in opposite signs. These features show again the role of the non-strange meson (σ, a_1) and strange meson (κ, K_1) exchanges. As a result, the net contribution from all the scalar and axial-vector meson exchanges and pomeron exchange in Ch.1 becomes weak and negative. This is clearly shown in Fig. 4(a), where V(SUM) has only a slight variation from V(Sum1). Similar features are also found for the Ch.3 central potentials of $V_{2\pi/\sigma}$,

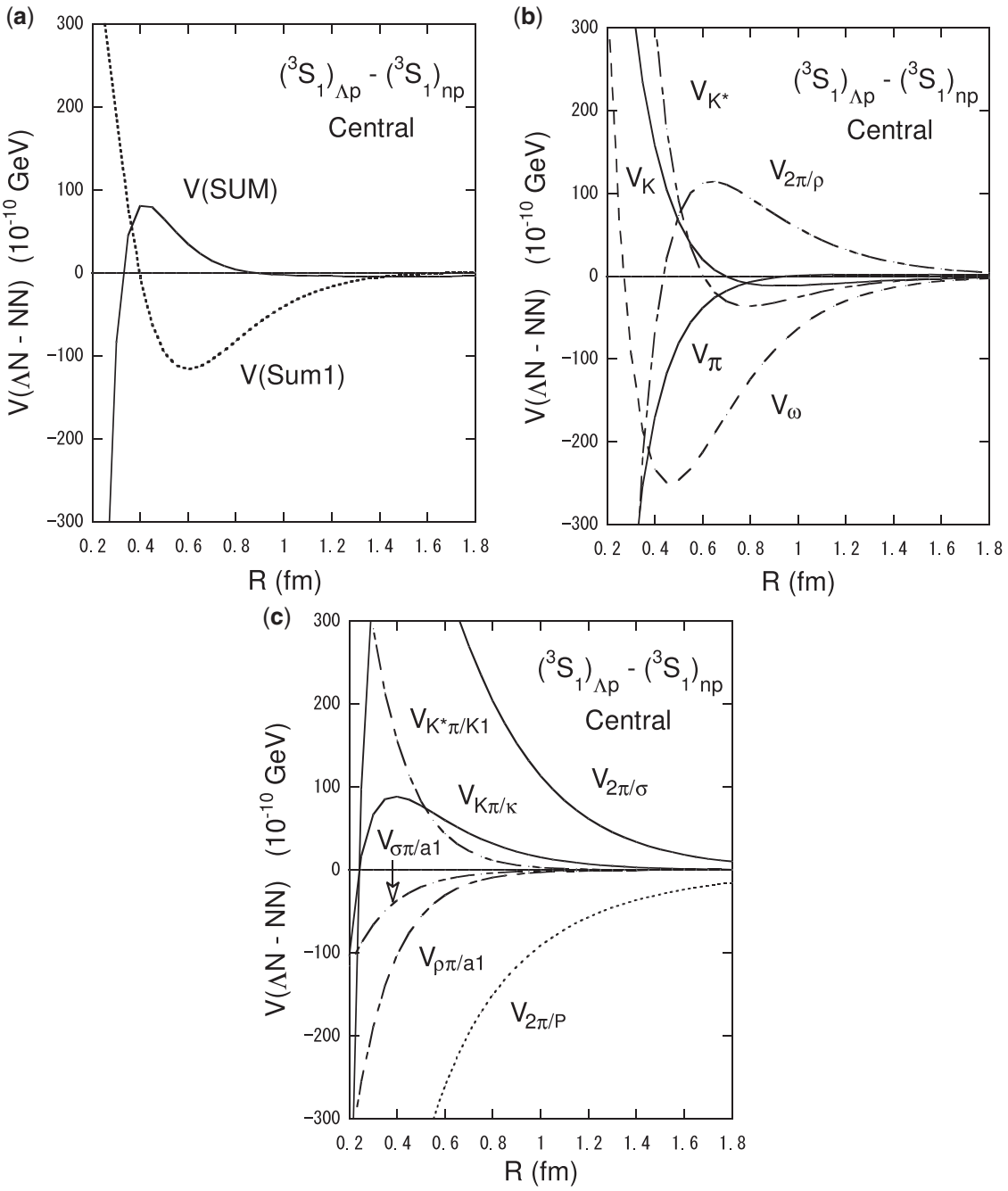

Fig. 6. (Ch. 3) The central-type weak decay transition potentials for the $(^3S_1)_{\Lambda p} \to (^3S_1)_{np}$ channel. Panels (a), (b), and (c) are the same as in Fig. 4.

$V_{2\pi/P}$, $V_{\rho\pi/a_1}$, $V_{\sigma\pi/a_1}$, and $V_{K^*\pi/K_1}$, as observed in Fig. 6(c). However, note that the behavior of $V_{K\pi/\kappa}$ in Ch.3 is different from that in Ch.1, since the $V_{K\pi/\kappa}$ potential in Ch.3 is positive. This difference comes from the strong isospin dependence as $c_0' + c_1'(\boldsymbol{\tau}_1 \cdot \boldsymbol{\tau}_2)$ of the $K\pi/\kappa$ exchange potential, where the isospin of the final NN is $T_{NN} = 0$ for Ch.3, while $T_{NN} = 1$ for Ch.1. Evidently the net contribution from the scalar and axial-vector meson and pomeron exchange potentials in Ch.3 becomes large and positive. As a result, the sign of the partial summed potential V(Sum1) has been changed in getting the total potential V(SUM), as shown in Fig. 6(a). It is notable that

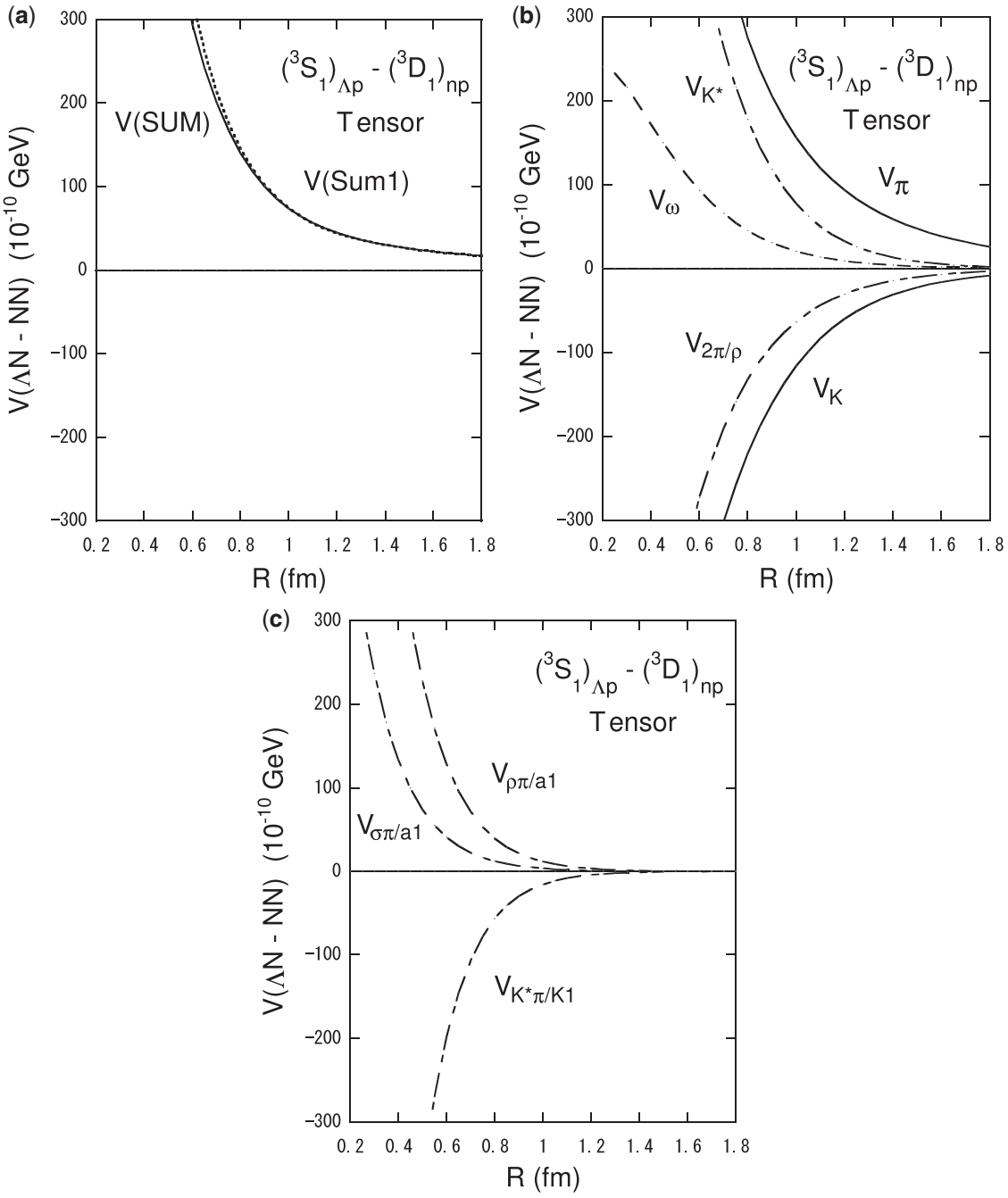

Fig. 7. (Ch.4) The tensor-type weak decay transition potentials for the $(^3S_1)_{\Lambda p} \rightarrow (^3D_1)_{np}$ channel. (a) V(Sum1) is the summed potential based on the $(\pi + K + 2\pi/\rho + K^* + \omega)$ meson exchanges, while V(SUM) is the total potential by summing V(Sum1) and the contributions of the axial-vector meson exchanges of $(\rho\pi/a_1 + \sigma\pi/a_1 + K^*\pi/K_1)$. (b) The transition potentials coming from the pseudoscalar mesons $(\pi + K)$ and the vector mesons $(2\pi/\rho + K^* + \omega)$. (c) The transition potentials coming from the axial-vector mesons $(\rho\pi/a_1 + \sigma\pi/a_1 + K^*\pi/K_1)$.

V(SUM) in Ch.3 is weakly positive and of short range. Figure 7(c) shows the obtained behaviors of the tensor potentials based on the axial-vector meson exchanges in Ch.4. It is clearly seen that the sum of $V_{\rho\pi/a_1} + V_{\sigma\pi/a_1}$ almost cancels the contribution of $V_{K^*\pi/K_1}$. Thus the net contribution of the

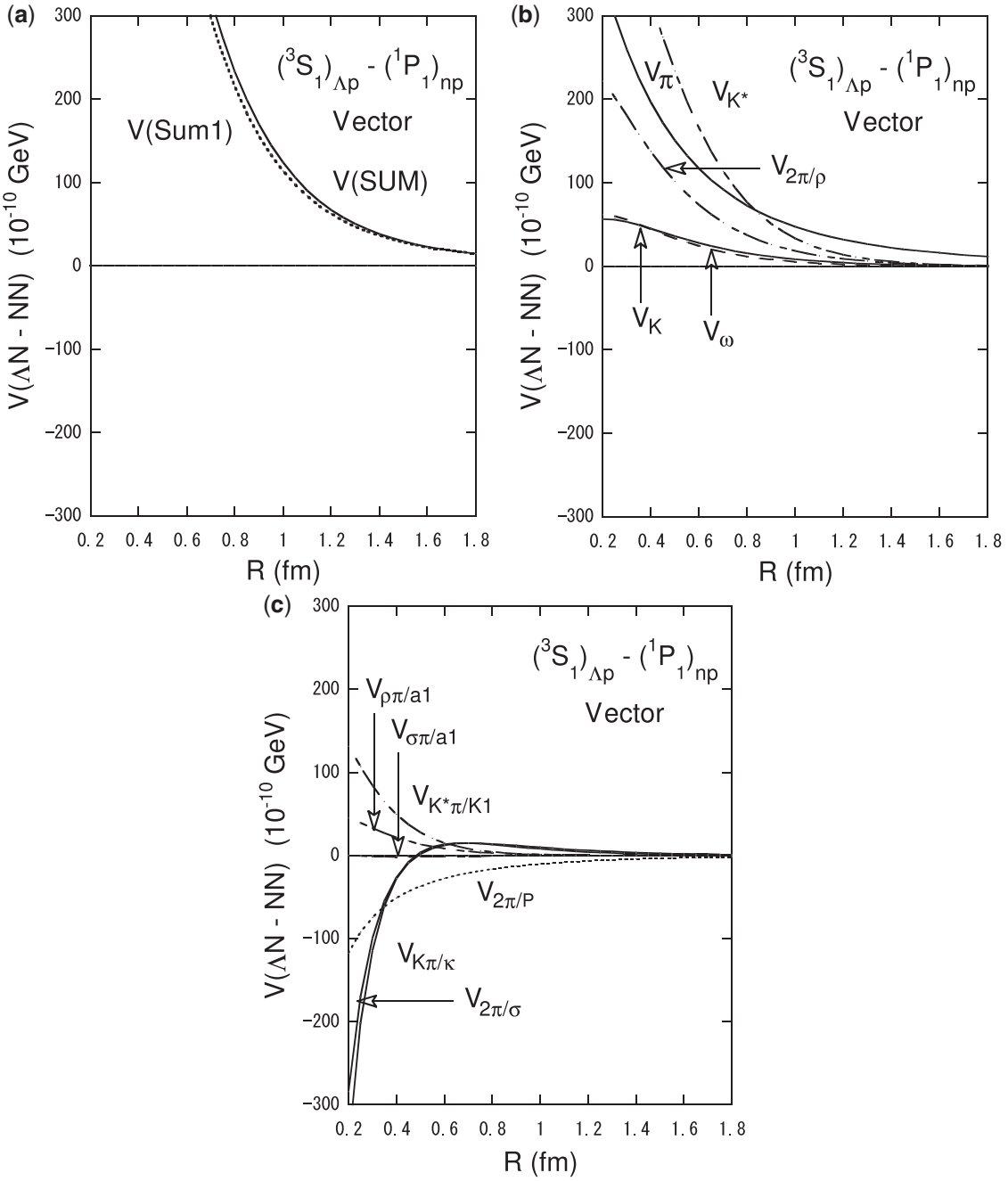

Fig. 8. (Ch.5) The parity-violating vector-type weak decay transition potentials for the $(^3S_1)_{\Lambda p} \rightarrow (^1P_1)_{np}$ channel. Panels (a), (b), and (c) are the same as in Fig. 4.

axial-vector meson exchanges turns out to be very small and negligible. This is reflected in Fig. 7(a), where V(SUM) is almost unchanged from V(Sum1).

The PV potentials of the scalar and axial-vector meson exchanges and the pomeron exchange in Ch.2 and Ch.5 are very weak and short ranged, which is reflected in very small variations of V(SUM) from V(Sum1) in Fig. 5(a) and Fig. 8(a). In Ch.6 of Fig. 9(b), the potentials of the scalar meson exchanges such as $V_{2\pi/\sigma}$ and $V_{K\pi/\kappa}$ show similar behavior and are positive at short range, and $V_{2\pi/P}$ is seen to be positive. The net contribution of the scalar meson and pomeron exchange potentials

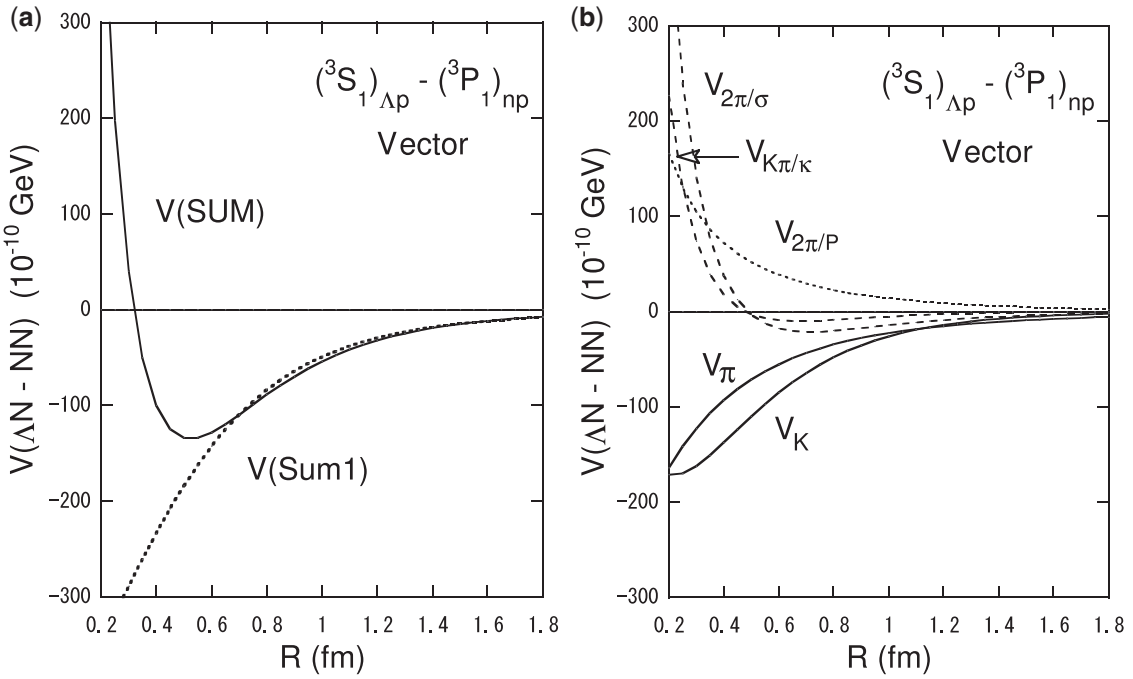

Fig. 9. (Ch.6) The parity-violating vector-type weak decay transition potentials for the $(^3S_1)_{\Lambda p} \to (^3P_1)_{np}$ channel. (a) V(Sum1) is the summed potential based on the $(\pi + K + 2\pi/\rho)$ meson exchanges, while V(SUM) is the total potential by summing, in addition to V(Sum1), all contributions from the other $(2\pi/\sigma + K\pi/\kappa + \rho\pi/a_1 + \sigma\pi/a_1 + K^*\pi/K_1)$ meson exchanges and the pomeron exchange $(2\pi/P)$. (b) The transition potentials coming from the pseudoscalar mesons $(\pi + K)$, the scalar mesons $(2\pi/\sigma, K\pi/\kappa)$, and the pomeron $2\pi/P$ exchange.

is positive at short range $R \lesssim 0.4$ fm, which causes a visible change of V(SUM) from V(Sum1) at short range, as shown in Fig. 9(a).

5. Estimates of non-mesonic weak decay rates and other observables

5.1. Calculated decay rates and comparison with experiments

We present the calculated results for the proton-stimulated decay rate $\Gamma_p(\Lambda p \to np)$, the neutron-stimulated one $\Gamma_n(\Lambda n \to nn)$, the ratio $\Gamma_n(\Lambda n \to nn)/\Gamma_p(\Lambda p \to np)$, the total decay rate $\Gamma_{\rm nm} = \Gamma_p(\Lambda p \to np) + \Gamma_n(\Lambda n \to nn)$, and the asymmetry parameter α_1 (or α_Λ) of the decay protons from the polarized hypernuclei. The intrinsic asymmetry parameter α_Λ from the polarized Λ hyperon in the nuclear medium is mostly discussed here, as α_Λ is often quoted and shown in the literature [11,26,47–49].

Table 3 summarizes the calculated decay rates, Γ_p, Γ_n, $\Gamma_{\rm nm}$, Γ_n/Γ_p, and the asymmetry parameter α_Λ for the typical hypernuclei of light s- and p-shell and medium-to-heavy mass systems. They are estimated on the basis of the weak decay potentials V(SUM) obtained for the six channels in the preceding section. The asymmetry parameter α_1 is calculated by Eq. (10), where Γ_1 is evaluated by Eq. (A.1) with the restriction of allowing $L_0 = 0$ only since the higher $L_0 \geq 2$ contributions to Γ_1 are small. The intrinsic asymmetry parameter α_Λ is related to α_1 by Eq. (25). The decay rates are given in units of the free Λ decay rate Γ_Λ $(= 2.50 \times 10^{-15}$ GeV). In Table II of Ref. [10] we reported the theoretical estimates of non-mesonic decay observables within some limitation of meson exchanges, while in this paper Table 3 presents the updated results obtained within the more comprehensive framework of the newly extended meson exchange potential models.

Table 3. Calculated decay rates, Γ_p, Γ_n, $\Gamma_{\rm nm}$, and Γ_n/Γ_p ratios, and intrinsic asymmetry parameter α_Λ of *s*- and *p*-shell and medium-to-heavy hypernuclei. The weak decay potentials V(SUM) of Eq. (42) for six decay channels are employed. For *p*-shell hypernuclei, the results with the simple shell-model wave functions are listed in parentheses, while the configuration-mixed wave functions are employed in the other cases. Calculations of α_Λ are done with restriction of $L_0 = 0$ only. The decay rates are given in units of the free Λ decay rate Γ_Λ. See the text.

	Γ_p	Γ_n	$\Gamma_{\rm nm}$	Γ_n/Γ_p	α_Λ
${}^{4}_{\Lambda}$H (0^+)	0.028	0.082	0.110	2.903	—
${}^{4}_{\Lambda}$He (0^+)	0.207	0.056	0.264	0.272	—
${}^{5}_{\Lambda}$He ($1/2^+$)	0.265	0.105	0.371	0.398	0.029
${}^{7}_{\Lambda}$Li ($1/2^+$)	0.345	0.161	0.506 [0.518]	0.469 [0.429]	0.389 [0.159]
${}^{8}_{\Lambda}$Li (1^-)	0.346	0.184	0.530 [0.534]	0.532 [0.530]	0.349 [0.301]
${}^{9}_{\Lambda}$Be ($1/2^+$)	0.450	0.184	0.634 [0.635]	0.410 [0.410]	0.064 [0.064]
${}^{10}_{\Lambda}$B (1^-)	0.507	0.187	0.693 [0.688]	0.368 [0.372]	0.240 [0.234]
${}^{10}_{\Lambda}$B* (2^-)	0.547	0.186	0.733 [0.725]	0.340 [0.340]	−0.024 [−0.026]
${}^{11}_{\Lambda}$B ($5/2^+$)	0.507	0.223	0.730 [0.729]	0.440 [0.447]	0.198 [0.223]
${}^{12}_{\Lambda}$B (1^-)	0.509	0.249	0.757 [0.746]	0.489 [0.500]	0.191 [0.269]
${}^{12}_{\Lambda}$C (1^-)	0.602	0.224	0.825 [0.830]	0.372 [0.378]	0.072 [0.069]
${}^{12}_{\Lambda}$C* (2^-)	0.602	0.214	0.815 [0.813]	0.355 [0.349]	0.068 [0.069]
${}^{13}_{\Lambda}$C ($1/2^+$)	0.558	0.233	0.792 [0.793]	0.418 [0.420]	0.078 [0.082]
${}^{14}_{\Lambda}$N (1^-)	0.624	0.235	0.859 [0.857]	0.376 [0.370]	0.104 [0.086]
${}^{15}_{\Lambda}$N ($3/2^+$)	0.627	0.263	0.889 [0.888]	0.419 [0.419]	0.088 [0.107]
${}^{16}_{\Lambda}$N*(1^-)	0.588	0.273	0.861 [0.863]	0.465 [0.464]	0.091 [0.081]
${}^{16}_{\Lambda}$O (0^-)	0.661	0.248	0.909 [0.902]	0.376 [0.365]	—
${}^{16}_{\Lambda}$O* (1^-)	0.661	0.248	0.909 [0.909]	0.376 [0.376]	0.057 [0.059]
${}^{28}_{\Lambda}$Si (2^+)	0.828	0.329	1.157	0.398	0.083
${}^{51}_{\Lambda}$V ($11/2^+$)	0.894	0.395	1.289	0.441	0.098
${}^{56}_{\Lambda}$Fe (1^-)	0.863	0.381	1.244	0.441	0.079
${}^{89}_{\Lambda}$Y ($7/2^-$)	0.876	0.400	1.276	0.456	0.087
${}^{139}_{\Lambda}$La ($9/2^+$)	0.857	0.428	1.285	0.499	0.067
${}^{209}_{\Lambda}$Bi ($9/2^+$)	0.833	0.450	1.283	0.540	0.066

The experimental data are summarized in Table 4, which should be compared with the calculated results listed in Table 3.

5.2. *Analyses of the roles of various meson exchanges*

Here we focus our attention on the particular roles of each meson exchange potential in getting the theoretical estimates of the non-mesonic decay rates and the decay asymmetry parameter α_1 (α_Λ). First, in Table 5 we compare the calculations of ${}^{5}_{\Lambda}$He with the experimental data. With the aim of understanding the asymmetry parameter α_1 (α_Λ), the separate contributions to α_1 (α_Λ) from the interference terms between the parity-conserving and the parity-violating amplitudes in Γ_1 in Eq. (A.1) are shown respectively in Table 6 for ${}^{5}_{\Lambda}$He.

We express $\Gamma_1 = A+B+C$ and the asymmetry parameter with the following symbolic expressions:

$$\alpha_1 = \frac{\Gamma_1}{\Gamma_0} = \frac{A+B+C}{\Gamma_0} = \frac{4\pi A + 4\pi B + 4\pi C}{\Gamma_p}, \tag{43}$$

$$A = {\rm Re}[ae^*], \quad B = {\rm Re}[-b(c-\sqrt{2}d)^*/\sqrt{3}], \quad C = {\rm Re}[-f(\sqrt{2}c+d)^*]. \tag{44}$$

Table 4. Summary of experimental data for Γ_p, Γ_n, $\Gamma_{\rm nm}$, and Γ_n/Γ_p, and the intrinsic asymmetry parameter α_Λ. The decay rates are given in units of the free Λ decay rate Γ_Λ. The data marked with a * are the weighted average for ${}^{12}_{\Lambda}$C and ${}^{11}_{\Lambda}$B hypernuclei.

	Γ_p	Γ_n	$\Gamma_{\rm nm}$	Γ_n/Γ_p	α_Λ	Ref.
${}^{4}_{\Lambda}$H			0.17 ± 0.11			[50,51]
${}^{4}_{\Lambda}$He	0.16 ± 0.02	$0.01^{+0.04}_{-0.01}$	0.17 ± 0.05	$0.06^{+0.28}_{-0.06}$		[50,51]
	0.16 ± 0.02	0.04 ± 0.02	0.20 ± 0.03	0.25 ± 0.13		[52]
	0.180 ± 0.028	≤ 0.035	0.177 ± 0.029	≤ 0.19		[53]
${}^{5}_{\Lambda}$He	0.21 ± 0.07	0.20 ± 0.11	0.41 ± 0.14	0.93 ± 0.55		[56]
			0.424 ± 0.024	$0.45 \pm 0.11^{+0.03}_{-0.03}$		[54,55]
					$0.11 \pm 0.08^{+0.04}_{-0.04}$	[48]
					$0.07 \pm 0.08^{+0.08}_{-0.00}$	[49]
					0.24 ± 0.22	[47]
	0.22 ± 0.05					[13]
		$0.125^{+0.066}_{-0.066}$		0.58 ± 0.32		[14]
${}^{7}_{\Lambda}$Li	0.28 ± 0.07					[13]
${}^{9}_{\Lambda}$Be	0.30 ± 0.07					[13]
${}^{11}_{\Lambda}$B				$1.04^{+0.59}_{-0.46}$		[56]
	0.30 ± 0.07		$0.95 \pm 0.13^{+0.04}_{-0.04}$	$2.16 \pm 0.58^{+0.45}_{-0.95}$		[57,58]
			$0.861 \pm 0.063^{+0.073}_{-0.073}$			[59]
	0.47 ± 0.11					[13]
		0.21 ± 0.16		0.46 ± 0.37		[14]
					$-0.20 \pm 0.26^{+0.04}_{-0.04}$*	[48]
					$-0.16 \pm 0.28^{+0.18}_{-0.00}$*	[49]
${}^{12}_{\Lambda}$C			1.14 ± 0.20	$1.33^{+1.12}_{-0.81}$		[56]
	0.31 ± 0.07		$0.89 \pm 0.15^{+0.03}_{-0.03}$	$1.87 \pm 0.59^{+0.32}_{-1.00}$		[57,58]
			$0.828 \pm 0.056^{+0.066}_{-0.066}$	$0.87 \pm 0.09^{+0.21}_{-0.21}$		[59]
			0.940 ± 0.035	$0.56 \pm 0.12^{+0.04}_{-0.04}$		[54]
					$-0.20 \pm 0.26^{+0.04}_{-0.04}$*	[48]
					$-0.16 \pm 0.28^{+0.18}_{-0.00}$*	[49]
				$0.51 \pm 0.13^{+0.05}_{-0.05}$		[60]
	0.45 ± 0.10	0.23 ± 0.08	0.68 ± 0.13	0.51 ± 0.14		[61,62]
	0.65 ± 0.19					[13]
		0.28 ± 0.12		0.58 ± 0.27		[14]
${}^{13}_{\Lambda}$C	0.60 ± 0.14					[13]
${}^{15}_{\Lambda}$N	0.49 ± 0.11					[13]
${}^{16}_{\Lambda}$O	0.44 ± 0.12					[13]
${}^{27}_{\Lambda}$Al			$1.230 \pm 0.062^{+0.032}_{-0.032}$			[59]
${}^{28}_{\Lambda}$Si			$1.125 \pm 0.067^{+0.106}_{-0.106}$	$0.79^{+0.13+0.25}_{-0.11-0.24}$		[59]
${}_{\Lambda}$Fe			1.21 ± 0.08	$1.13^{+0.18+0.22}_{-0.15-0.24}$		[59]

The quantities A, B, and C are defined such that, for example, $A = \mathrm{Re}[ae^*]$ signifies the integrated value of the term which contains the amplitude $\mathrm{Re}(ae^*)$ in Γ_1 of Eq. (A.1), and this term corresponds to $\mathrm{Re}\langle -ae^*\rangle$ of $\alpha_\Lambda^{\rm elem}$ in Eq. (26). The apparent sign difference between $A = \mathrm{Re}[ae^*]$ and $\mathrm{Re}\langle -ae^*\rangle$ is understandable from the decay kinematics originated in the nuclear medium for the quantity A and has been explained in Ref. [10]. The two quantities should have the same property. Therefore, intuitively, it is all right to consider the expression of A as $\sim$ "$\mathrm{Re}[-ae^*]$" in opposite sign, like $\mathrm{Re}\langle -ae^*\rangle$ in $\alpha_\Lambda^{\rm elem}$ as far as the sign is concerned. Likewise, B and C are the integrated values of the interference terms which contain the amplitudes of $\mathrm{Re}\{-b(c - \sqrt{2}d)^*/\sqrt{3}\}$

Table 5. Calculated decay rates $\Gamma_{\rm nm}$, Γ_n/Γ_p, and asymmetry parameter α_Λ of ${}^{5}_{\Lambda}$He for the four stages of the weak decay potentials are compared with the experimental data. The decay rates are given in units of the free Λ decay rate Γ_Λ. The abbreviation (ps+vec) = "$\pi + K + 2\pi/\rho + K^* + \omega$" is used. The value marked ** is the one-nucleon induced decay rate.

	$\Gamma_{\rm nm}$	Γ_n/Γ_p	$\alpha_\Lambda = \alpha_1$
I: π	0.260	0.109	-0.417
II: (ps+vec)	0.315	0.417	0.141
III: (ps+vec) + $2\pi/\sigma + K\pi/\kappa + 2\pi/P$	0.372	0.409	0.032
IV: (ps+vec) + $2\pi/\sigma + K\pi/\kappa + 2\pi/P$ + $\rho\pi/a_1 + \sigma\pi/a_1 + K^*\pi/K_1$	0.371	0.398	0.029
Exp. [54,55]	0.424 ± 0.024	$0.45 \pm 0.11^{+0.03}_{-0.03}$	
Exp. [48]			$0.11 \pm 0.08^{+0.04}_{-0.04}$
Exp. [49]			$0.07 \pm 0.08^{+0.08}_{-0.00}$
Exp. [47]			0.24 ± 0.22
Exp. [14]	0.342 ± 0.078**	0.58 ± 0.32	
Chumillas et al. [23]	0.388	0.415	0.041

Table 6. The separate contributions of the $A = \mathrm{Re}[ae^*]$, $B = \mathrm{Re}[-b(c-\sqrt{2})^*/\sqrt{3}]$, and $C = \mathrm{Re}[-f(\sqrt{2}c+d)^*]$ parts to Γ_1 in Eq. (43), Γ_1, Γ_0, and α_Λ of ${}^{5}_{\Lambda}$He for the four stages of the weak decay potentials are compared with the experimental data. The decay rates are given in units of the free Λ decay rate Γ_Λ. (ps+vec) = "$\pi + K + 2\pi/\rho + K^* + \omega$."

	$4\pi A$	$4\pi B$	$4\pi C$	$4\pi\Gamma_1$	$4\pi\Gamma_0$	$\alpha_\Lambda = \alpha_1$
I: π	0.0012	0.012	-0.111	-0.098	0.234	-0.417
II: (ps+vec)	0.110	0.013	-0.091	0.032	0.222	0.141
III: (ps+vec)+ $2\pi/\sigma + K\pi/\kappa + 2\pi/P$	0.140	-0.0022	-0.129	0.0086	0.264	0.032
IV: (ps+vec)+ $2\pi/\sigma + K\pi/\kappa + 2\pi/P$ + $\rho\pi/a_1 + \sigma\pi/a_1 + K^*\pi/K_1$	0.138	-0.0021	-0.128	0.0078	0.265	0.029
Exp. [48]						$0.11 \pm 0.08^{+0.04}_{-0.04}$
Exp. [49]						$0.07 \pm 0.08^{+0.08}_{-0.00}$
Exp. [47]						0.24 ± 0.22

and $\mathrm{Re}\{-f(\sqrt{2}c+d)^*\}$ in Γ_1 of Eq. (A.1), respectively. These correspond to $\mathrm{Re}\langle b(c-\sqrt{2}d)^*/\sqrt{3}\rangle$ and $\mathrm{Re}\langle f(\sqrt{2}c+d)^*\rangle$ of $\alpha_\Lambda^{\rm elem}$ in Eq. (26), respectively. The signs of the B and C terms are also understandable.

Note that in the calculations the transition amplitudes such as $c({}^3S_1 \to {}^3S_1)$, $d({}^3S_1 \to {}^3D_1)$, $e({}^3S_1 \to {}^1P_1)$, and $f({}^3S_1 \to {}^3P_1)$ are modified owing to the initial ΛN tensor correlation for the $({}^3S_1)_{\Lambda N}$ state and the final NN tensor correlations for the $({}^3S_1)_{NN}$ and $({}^3D_1)_{NN}$ states.

The calculations are carried out step by step by introducing the meson exchange potentials successively. We take four stages of calculations corresponding to four different combinations of the weak decay potentials. They are classified as stage I: V_π only; stage II: potentials of the pseudoscalar and vector meson exchanges, which we denote as "(ps+vec)." Then stage III also contains the potentials of scalar meson exchanges and the pomeron exchanges, and in stage IV all contributions are added. Thus we discuss the calculated results following these four categories, noting that II and IV correspond to the potentials V(Sum1) and V(SUM), respectively, presented in the preceding section.

$$\begin{aligned}
&\text{I} : \pi \text{ only} \\
&\text{II} : (\text{ps+vec}) \equiv (\pi + K + 2\pi/\rho + K^* + \omega) \longleftrightarrow V(\text{Sum1}) \\
&\text{III} : (\text{ps+vec}) + 2\pi/\sigma + K\pi/\kappa + 2\pi/P \\
&\text{IV} : (\text{ps+vec}) + 2\pi/\sigma + K\pi/\kappa + 2\pi/P + \rho\pi/a_1 + \sigma\pi/a_1 + K^*\pi/K_1 \longleftrightarrow V(\text{SUM}).
\end{aligned} \tag{45}$$

First of all, the case of the one-π exchange potential only is shown in the second line in Table 5. This case predicts a small Γ_n/Γ_p ratio and large negative α_Λ, which disagree with the data. This feature is well known and is understood in terms of the very strong tensor force of V_π. In Table 6, it is shown in the second line that the large α_Λ comes from the large C term for which Re$[-f(\sqrt{2}c + d)^*]$ ∼ "Re$[f(\sqrt{2}c + d)^*]$" is negative due to the dominant contribution of Re(fd^*) being $f < 0$ and $d \approx d_0(^3S_1 \to {}^3D_1) > 0$. It is noted that the amplitude d is expressed as

$$\begin{aligned}
d(^3S_1 \to {}^3D_1) = {} & d_0(^3S_1 \to {}^3D_1) + d_1(\text{induced } {}^3D_1 \to {}^3D_1) \\
& + d_2(^3S_1 \to \text{induced } {}^3S_1) + d_3(\text{induced } {}^3D_1 \to \text{induced } {}^3S_1),
\end{aligned} \tag{46}$$

when the ISC for ΛN in $^3S_1$ and the FSC for NN in $^3D_1$ are properly considered. In the case of the strong tensor force in V_π, $d \approx d_0(^3S_1 \to {}^3D_1)$ holds when the ISC is not large.

Next are the calculated results in stage II quoted as (ps+vec) = "$\pi + K + 2\pi/\rho + K^* + \omega$," which are shown in Tables 5 and 6. The decay rate $\Gamma_{\rm nm}$ and the ratio Γ_n/Γ_p are improved, but the α_Λ value is a little overestimated. The results are understandable from the decay potential of $V(\text{Sum1}) = V_\pi + V_K + V_{2\pi/\rho} + V_{K^*} + V_\omega$, which has the following characteristics: (a) The central potentials of Ch.1 ($^1S_0 \to {}^1S_0$) and Ch.3 ($^3S_1 \to {}^3S_1$) are strong and negative. (b) The tensor potential of Ch.4 ($^3S_1 \to {}^3D_1$) becomes weaker compared with the V_π potential alone. (c) The parity-violating potentials of Ch.2 ($^1S_0 \to {}^3P_0$) and Ch.5 ($^3S_1 \to {}^1P_1$) are strong, though their signs are opposite. The potential of Ch.6 ($^3S_1 \to {}^3P_1$) is strong and negative. [See Figs. 4(a)–9(a).] These features of $V(\text{Sum1})$ enhance the decay rate and the Γ_n/Γ_p ratio and make α_Λ positive. The separate contributions of the A, B, and C terms to α_Λ are listed in the third line of Table 6.

The results obtained in stage III are shown in the fourth line in Tables 5 and 6. The calculated observables $\Gamma_{\rm nm}$, Γ_n/Γ_p, and α_Λ seem to be good compared with the data. This shows the special effect of adding the potentials of the scalar mesons and pomeron exchanges to $V(\text{Sum1})$ of the (ps+vec) exchanges. The "scalar-meson + pomeron" exchanges modify the central potentials of Ch.1 ($^1S_0 \to {}^1S_0$) and Ch.3 ($^3S_1 \to {}^3S_1$) in particular. The potential of Ch.1 becomes a little stronger than $V(\text{Sum1})$ with negative sign, while the potential of Ch.3 turns out to be positive in sign, which is different behavior from $V(\text{Sum1})$ in Ch.3. The difference between the potential in Ch.1 and that in Ch.3 is attributed to the different behavior of the $V_{K\pi/\kappa}$ potential for Ch.1 and Ch.3, as seen in Figs. 4(b) and 6(b), since $V_{K\pi/\kappa}$ has an isospin dependence of $c_0' + c_1'(\boldsymbol{\tau}_1 \cdot \boldsymbol{\tau}_2)$ and the isospin $T_{NN} = 1$ for Ch.1 and $T_{NN} = 0$ for Ch.3. The parity-violating potentials of Ch.6 ($^3S_1 \to {}^3P_1$) are modified at short ranges of $R \lesssim 0.6$ fm, as seen in Fig. 9(b).

The variation of the central potential in Ch.1 makes the transition amplitude $a(^1S_0 \to {}^1S_0)$ larger in negative sign, and then makes $A \sim$ "Re$[-ae^*]$" larger in positive sign, as seen in the fourth line in Table 6. The variation of the central potential in Ch.3 changes the amplitudes $c(^3S_1 \to {}^3S_1)$ and $d(^3S_1 \to {}^3D_1)$ from those in case 3. The amplitude c is expressed as

$$\begin{aligned}
c(^3S_1 \to {}^3S_1) = {} & c_0(^3S_1 \to {}^3S_1) + c_1(\text{induced } {}^3D_1 \to {}^3S_1) \\
& + c_2(^3S_1 \to \text{induced } {}^3D_1) + d_3(\text{induced } {}^3D_1 \to \text{induced } {}^3D_1).
\end{aligned} \tag{47}$$

Table 7. Channel contributions to $\Gamma_p(\Lambda p \to np)$ and $\Gamma_n(\Lambda n \to nn)$ for ${}^{5}_{\Lambda}$He estimated in stage IV, i.e. V(SUM). The decay rates are given in units of the free Λ decay rate Γ_Λ.

	${}^1S_0 \to {}^1S_0$	${}^1S_0 \to {}^3P_0$	${}^3S_1 \to {}^3S_1$	${}^3S_1 \to {}^3D_1$	${}^3S_1 \to {}^1P_1$	${}^3S_1 \to {}^3P_1$	Sum
Γ_p	0.019	0.0011	0.051	0.017	0.144	0.033	0.265
Γ_n	0.037	0.0022	—	—	—	0.066	0.105

$(\Gamma_{\rm nm} = \Gamma_p + \Gamma_n = 0.371\,\Gamma_\Lambda)$

When the ISC is not large, $c \approx c_0({}^3S_1 \to {}^3S_1) + c_2({}^3S_1 \to \text{induced } {}^3D_1)$. In the present case, c_0 becomes positive and c_2 is also positive, resulting in c being positive and large. The amplitude d is expressed in Eq. (46), and $d \approx d_0({}^3S_1 \to {}^3D_1) + d_2({}^3S_1 \to \text{induced } {}^3S_1)$. d_0 is positive, while d_2 becomes negative since the induced ${}^3S_1$ wave $i^0\chi_0(k,r)$ in the FSC is negative over the effective interaction range [1], resulting in d being positive but not large. These features explain that $C \sim$ "Re$[f(\sqrt{2}c + d)^*]$" is negative and large, and $B \sim$ "Re$[b(c - \sqrt{2}d)^*/\sqrt{3}]$" is negative but small. Consequently α_Λ is reduced to a small value, as seen in the fourth line in Table 6.

Finally, in stage IV, the calculations are performed with the potential V(SUM) of "all mesons and pomeron" exchanges, so that the potential V(SUM) in each decay channel shown in Figs. 4(a)–9(a) is adopted. The calculated values are listed in the fifth line in Tables 5 and 6, and these final results should be compared with the experimental data. The potential V(SUM) includes the contributions from the axial-vector meson exchanges. However, the contributions of potentials from the axial-vector meson exchanges in each channel are found to be small. Actually, $V_{\rho\pi/a_1} + V_{\sigma\pi/a_1}$ for the non-strange meson a_1 exchange and $V_{K^*\pi/K_1}$ for the strange meson K_1 exchange tend to cancel each other out for the PC central and tensor-force channels, as seen in Figs. 4(c), 6(c), and 7(c). The PV potentials themselves of the a_1 and K_1 exchanges are very weak and negligible, as seen in Figs. 5(c) and 8(c). Thus the effect of the axial-vector meson exchanges on the total potential V(SUM) is not large and, therefore, the calculated values of the observables for stage IV of the "pseudoscalar + vector + scalar + axial-vector" mesons plus pomeron exchanges exhibit only small variations from those of stage III, the "pseudoscalar + vector + scalar" mesons plus pomeron exchanges. It is verified that the present model of "pseudoscalar + vector + scalar + axial-vector" mesons plus pomeron exchanges for the weak decay interaction can explain the experimental data well.

In Table 7 we show separate channel contributions to the proton-stimulated decay rate $\Gamma_p(\Lambda p \to np)$ and the neutron-stimulated one $\Gamma_n(\Lambda n \to nn)$. It can be seen in Table 7 that Ch.3 (${}^3S_1 \to {}^3S_1$), Ch.5 (${}^3S_1 \to {}^1P_1$), and Ch.6 (${}^3S_1 \to {}^3P_1$) contribute dominantly to Γ_p, while Ch.6 (${}^3S_1 \to {}^3P_1$) contributes to Γ_n to a large extent. Such a contribution of Ch.3 to Γ_p is understood by the amplitude $c({}^3S_1 \to {}^3S_1) \approx c_0({}^3S_1 \to {}^3S_1) + c_2({}^3S_1 \to \text{induced } {}^3D_1)$, which is big due to the c_2 term of the tensor force and induced $i^2\chi_2(k,r)$ coming from the FSC of the strong tensor correlation [1], and other contributions to Γ_p mentioned above can be recognized from the channel potentials depicted in Figs. 8(a) and 9(a). Another noticeable point is that the summed decay rate of PV channels, i.e. "$({}^3S_1)_{\Lambda N} \to ({}^1P_1)_{NN}$ plus $({}^3S_1)_{\Lambda N} \to ({}^3P_1)_{NN}$," amounts to $0.243\,\Gamma_\Lambda$, which is as large as 65% of the total decay rate $\Gamma_{\rm nm} = 0.371\,\Gamma_\Lambda$ for the non-mesonic weak decay of ${}^{5}_{\Lambda}$He.

Table 8 shows the calculated decay rates and asymmetry parameter of ${}^{12}_{\Lambda}$C(1^-) for four stages of different combinations of the meson exchanges. As in the case of ${}^{5}_{\Lambda}$He decay, the stage III and IV calculations of $\Gamma_{\rm nm}$ and Γ_n/Γ_p and the asymmetry parameter α_Λ for ${}^{12}_{\Lambda}$C lead to almost the same results, as shown in the fourth and fifth lines, respectively, of Table 8. The model of "(ps+vec)

Table 8. Calculated decay rates, $\Gamma_{\rm nm}$, Γ_n/Γ_p, and asymmetry parameter α_Λ of ${}^{12}_{\Lambda}{\rm C}(1^-)$ for the four stages of the weak decay potentials are compared with the experimental data. The configuration-mixed nuclear SM + Λ hyperon wave function is adopted. The decay rates are given in units of the free Λ decay rate Γ_Λ. The data marked with a * are the weighted average for ${}^{12}_{\Lambda}{\rm C}$ and ${}^{11}_{\Lambda}{\rm B}$ hypernuclei. The values marked ** are the one-nucleon induced decay rates.

	$\Gamma_{\rm nm}$	Γ_n/Γ_p	$\alpha_\Lambda = -\frac{J_H+1}{J_H}\alpha_1$
I: π	0.578	0.102	-0.339
II: (ps+vec)	0.690	0.382	0.162
III: (ps+vec) + $2\pi/\sigma + K\pi/\kappa + 2\pi/P$	0.830	0.384	0.075
IV: (ps+vec) + $2\pi/\sigma + K\pi/\kappa + 2\pi/P$ + $\rho\pi/a_1 + \sigma\pi/a_1 + K^*\pi/K_1$	0.825	0.372	0.072
Exp. [59]	$0.828 \pm 0.056^{+0.066}_{-0.066}$	$0.87 \pm 0.09^{+0.21}_{-0.21}$**	
Exp. [54]	0.940 ± 0.035	$0.56 \pm 0.12^{+0.04}_{-0.04}$	
Exp. [48]			$-0.20 \pm 0.26^{+0.04}_{-0.04}$*
Exp. [49]			$-0.16 \pm 0.28^{+0.18}_{-0.00}$*
Exp. [60]		$0.51 \pm 0.13^{+0.05}_{-0.05}$	
Exp. [61,62]	0.68 ± 0.13**	0.51 ± 0.14	
Exp. [14]	0.77 ± 0.15**	0.58 ± 0.27	
Chumillas *et al.* [23]	0.722	0.366	-0.207

Table 9. Channel contributions to $\Gamma_p(\Lambda p \to np)$ and $\Gamma_n(\Lambda n \to nn)$ for ${}^{12}_{\Lambda}{\rm C}(1^-)$ estimated in stage IV, i.e. V(SUM). The configuration-mixed SM + Λ hyperon wave function is adopted. The decay rates are given in units of the free Λ decay rate Γ_Λ.

	${}^1S_0 \to {}^1S_0$	${}^1S_0 \to {}^3P_0$	${}^3S_1 \to {}^3S_1$	${}^3S_1 \to {}^3D_1$	${}^3S_1 \to {}^1P_1$	${}^3S_1 \to {}^3P_1$	Sum
Γ_p	0.049	0.0021	0.112	0.039	0.327	0.073	0.602
Γ_n	0.098	0.0040	—	—	—	0.121	0.223

($\Gamma_{\rm nm} = \Gamma_p + \Gamma_n = 0.825\,\Gamma_\Lambda$)

$+ 2\pi/\sigma + K\pi/\kappa + 2\pi/P + \rho\pi/a_1 + \sigma\pi/a_1 + K^*\pi/K_1$" exchanges can explain the experimental data of ${}^{12}_{\Lambda}{\rm C}$ well within the error bars.

In Table 9 the separate channel contributions to $\Gamma_p(\Lambda p \to np)$ and $\Gamma_n(\Lambda n \to nn)$ are shown. It can again be seen in Table 9 that Ch.3 (${}^3S_1 \to {}^3S_1$), Ch.5 (${}^3S_1 \to {}^1P_1$), and Ch.6 (${}^3S_1 \to {}^3P_1$) contribute dominantly to Γ_p, while Ch.6 (${}^3S_1 \to {}^3P_1$) contributes to Γ_n to a large extent. The summed decay rate of PV channels, i.e. "$({}^3S_1)_{\Lambda N} \to ({}^1P_1)_{NN}$ plus $({}^3S_1)_{\Lambda N} \to ({}^3P_1)_{NN}$," amounts to as much as 63% of the total decay rate $\Gamma_{\rm nm} = 0.825\,\Gamma_\Lambda$ for the non-mesonic weak decay of ${}^{12}_{\Lambda}{\rm C}$.

It is interesting to note that in Table 3 the p-shell hypernuclei with odd Z such as ${}_\Lambda$Li, ${}_\Lambda$B, and ${}_\Lambda$N isotopes are calculated to have a large asymmetry parameter α_Λ for the angular distribution of emitted protons due to the decay kinematics.

5.3. *Calculated lifetimes up to heavy hypernuclei*

The hypernuclear lifetimes can be estimated from the weak decay rates of Γ_π and $\Gamma_{\rm nm}$ by the relation $\tau = \hbar/(\Gamma_\pi + \Gamma_{\rm nm})$. The evaluated lifetimes are compared with the available experimental data [15–18,34,50,51,56,65–71] in Table 10 and Fig. 10. The mesonic decay rates Γ_π are taken from our works, Refs. [63,64]. Some values marked by an asterisk (*) in Table 10 are substituted values from calculations for other hypernuclei or other spin states. That is, we substitute the numbers of ${}^{16}_{\Lambda}{\rm O}(1^-)$,

Table 10. Calculated hypernuclear weak decay rates and lifetimes for *s*- and *p*-shell, and medium-to-heavy hypernuclei. The decay rates are given in units of the free Λ decay rate Γ_Λ. The lifetimes are given in picoseconds. Experimental data of lifetimes are listed for comparison. The data marked ** are for the hyperfragments whose masses are not specified. See the text.

	Γ_π	$\Gamma_{\rm nm}$	$\Gamma_\pi + \Gamma_{\rm nm}$	τ	$\tau^{\rm exp}$	
${}^{3}_{\Lambda}$H					217^{+19}_{-16}	[15]
					183^{+42}_{-32}	[16]
					155^{+25}_{-22}	[17]
					181^{+54}_{-39}	[18]
${}^{4}_{\Lambda}$H	0.891	0.110	1.001	262.7	194^{+24}_{-26}	[50,51]
					194^{+20}_{-18}	[15]
					140^{+48}_{-33}	[16]
${}^{4}_{\Lambda}$He	0.658	0.264	0.922	285.2	256 ± 27	[50,51]
					245 ± 24	[53]
${}^{5}_{\Lambda}$He	0.608	0.371	0.979	268.6	256 ± 21	[56]
					273^{+11}_{-10}	[65]
${}^{11}_{\Lambda}$B	0.316	0.730	1.046	251.4	192 ± 22	[66]
					211 ± 13	[67]
${}^{12}_{\Lambda}$C	0.228	0.825	1.053	249.8	211 ± 31	[66]
					231 ± 15	[67–69]
${}^{16}_{\Lambda}$O	0.074*	0.909	0.983	267.5	86^{+33}_{-26}	[70]
${}^{27}_{\Lambda}$Al					203 ± 10	[67]
${}^{28}_{\Lambda}$Si	0.088	1.157	1.245	211.2	206 ± 12	[67–69]
$A \simeq 28 \pm 7$					212.2 ± 3.5**	[34]
$A \simeq 32 \pm 8$					201.1 ± 49.3**	[34]
${}^{51}_{\Lambda}$V	0.02*	1.289	1.309	200.9		
$A \simeq 54 \pm 16$					209.5 ± 4.5**	[34]
${}^{56}_{\Lambda}$Fe	0.02*	1.244	1.264	208.1	215 ± 14**	[67–69]
${}^{89}_{\Lambda}$Y	0.005*	1.276	1.281	205.3		
$A \simeq 100 \pm 30$					220.5 ± 45.6**	[34]
${}^{139}_{\Lambda}$La	0.005*	1.285	1.290	203.9		
${}^{209}_{\Lambda}$Bi	0.005*	1.283	1.288	204.2	250^{+250}_{-100}	[71]

${}^{57}_{\Lambda}$Ni, ${}^{57}_{\Lambda}$Ni, ${}^{91}_{\Lambda}$Zr, ${}^{139}_{\Lambda}$Ba, and ${}^{209}_{\Lambda}$Pb for ${}^{16}_{\Lambda}$O(0^-), ${}^{51}_{\Lambda}$V, ${}^{56}_{\Lambda}$Fe, ${}^{89}_{\Lambda}$Y, ${}^{139}_{\Lambda}$La, and ${}^{209}_{\Lambda}$Bi, respectively. One sees in Table 10 and in Fig. 10 that the calculated lifetimes explain the general trend of experimental data fairly well, and give the saturated value at the medium-to-heavy mass systems; however, the evaluated τ are somewhat overestimated to larger values compared to the data for light *s*- and *p*-shell hypernuclei. The overshooting of the evaluated lifetimes of the light hypernuclei could be due to the fact that our non-mesonic decay rates $\Gamma_{\rm nm}$ are calculated exclusively as one-nucleon induced ones as $\Gamma_{\rm nm} = \Gamma_p(\Lambda p \to np) + \Gamma_n(\Lambda n \to nn)$, and do not include contributions from the two-nucleon induced decay rate Γ_{2N}, which is known to exist.

5.4. Additional comments on the roles of two-meson exchanges

We note that the strong baryon–baryon–meson (BBM) coupling constants are taken from the ESC08c model, and how to determine the MMM coupling constants was already described in Sect. 4.2. On the other hand, we treat the pi–pi–pomeron coupling constant $g_{\pi\pi P}$ as an adjustable parameter in order to reproduce the α_Λ value observed for ${}^{5}_{\Lambda}$He, because we found that the calculated asymmetry parameter α_Λ depends sensitively on the $g_{\pi\pi P}$ value and also because the experimental errors for α_Λ (${}^{5}_{\Lambda}$He) are small enough to give a good restriction [48,49] (cf. Table 4). This situation is demonstrated

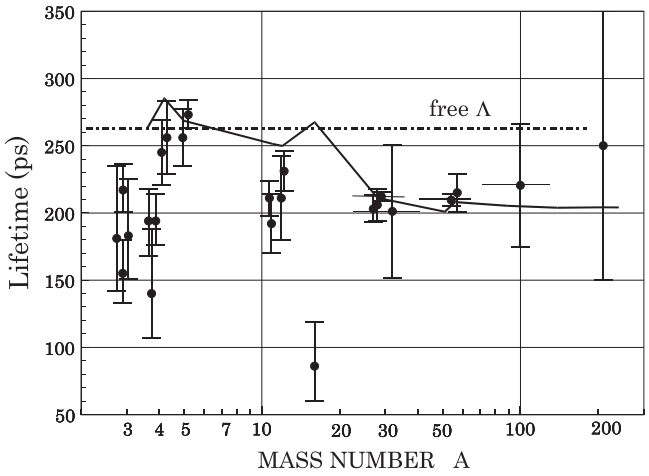

Fig. 10. The hypernuclear lifetimes calculated in the present model (solid line) and the experimental data compared as a function of mass number. The lifetime of a free Λ is shown by the dash-dotted line. Lifetimes are in picoseconds.

Table 11. The parameter $g_{\pi\pi P}$ dependence on the decay rate, the decay rate ratio, and the asymmetry parameter for ${}^{5}_{\Lambda}$He, which is used to fix $g_{\pi\pi P}$. The resultant predictions for ${}^{12}_{\Lambda}$C are also listed for reference. The decay rates are given in units of the free Λ decay rate Γ_Λ.

	${}^{5}_{\Lambda}$He			${}^{12}_{\Lambda}$C		
$g_{\pi\pi P}$	$\Gamma_{\rm nm}$	Γ_n/Γ_p	α_Λ	$\Gamma_{\rm nm}$	Γ_n/Γ_p	α_Λ
−4050.0 MeV	0.372	0.384	−0.024	0.825	0.353	0.024
−4280.0 MeV	0.371	0.398	0.029	0.825	0.372	0.072
−4460.0 MeV	0.371	0.409	0.072	0.827	0.387	0.110

in Table 11, where the calculated weak NM decay observables of ${}^{5}_{\Lambda}$He and ${}^{12}_{\Lambda}$C are compared for the three choices of $g_{\pi\pi P}$. Here one sees that the decay rates $\Gamma_{\rm nm}$ and Γ_n/Γ_p do not change much, while the asymmetry parameter α_Λ varies noticeably within the chosen range of $g_{\pi\pi P}$. Thus we have adopted the optimum value $g_{\pi\pi P} = -4280.0$ MeV so as to be consistent with the experimental data of α_Λ. For the experimental values one may refer to Tables 5 and 8, respectively. We also remark that the optimum $g_{\pi\pi P}$ value is correlated mostly with the $g_{\pi\pi\sigma}$ one, which has been fixed in previous works [10,26].

It is interesting to compare the present results with those of the Chumillas et al. model [23] in which the meson exchanges are expressed symbolically by OME(ps+vec) + $2\pi/\sigma + 2\pi$. In the present case the coverage of the meson exchanges to be compared are shown by stages III and IV of Eq. (45). Both models take account of the common exchange effects of the SU(3) octet of pseudoscalar and vector mesons, although the treatments are certainly different from each other. As the OME model cannot explain the small α_Λ observed in ${}^{5}_{\Lambda}$He and ${}^{12}_{\Lambda}$C, Chumillas et al. [23] introduced the correlated and uncorrelated 2π exchange effects, achieving satisfactory results. In the present case, because the net effect of axial-vector meson exchanges (a_1 and K_1) in stage IV is small, as discussed previously, the main part of our model is maintained by stage III, which consists of (ps+vec) + $2\pi/\sigma + K\pi/\kappa + 2\pi/P$. Thus we know that the sum of the three potential parts $V_{2\pi/\sigma} + V_{K\pi/\kappa} + V_{2\pi/P}$ would possibly have similar roles to the $V_{2\pi/\sigma} + V^{\rm uncorrel}_{2\pi}$ potential of Chumillas et al. It should be noted that our model treats the potentials due to the non-strange meson and the strange meson exchanges symmetrically

even in the scalar meson sector, like the treatment in the pseudoscalar, vector, and axial-vector meson sectors.

6. Summary and conclusions

In order to construct the weak $\Lambda N \to NN$ two-body potentials for hypernuclear non-mesonic weak decay (NMWD), the previous framework of a potential model has been systematically extended to include various correlated two-meson exchanges. Exchanges of pseudoscalar, vector, scalar, and axial-vector mesons and also the pomeron have been taken into account, so that both non-strange and strange meson members have been considered equally and symmetrically to form as completely in quantum number $J^{\rm PC}$ as possible. The present framework is based on the newest attainment for the strong coupling constants for the baryon–baryon–meson vertices of the Nijmegen ESC08c model (2016 version) by replacing it partly with a possible weak interaction vertex.

First we obtained the overall explanation and satisfactory agreement with the experimental weak non-mesonic decay observables such as the decay rates $\Gamma_{\rm nm}$, the ratios Γ_n/Γ_p, the asymmetry parameters α_Λ, and the hypernuclear lifetimes τ for the light to medium-to-heavy mass systems. The theoretical estimates are presented in tables in comparison with the experimental values. The partial decay rates $\Gamma_p(\Lambda p \to np)$ and $\Gamma_n(\Lambda n \to nn)$ were studied by divided channel contributions, assuming that the decays occur from the initial ΛN in a relative S-state. It is notable that the theoretical asymmetry parameter α_Λ is sensitive to the $g_{\pi\pi P}$ coupling constant, although the estimates of the total decay rates $\Gamma_{\rm nm}$ and the ratios Γ_n/Γ_p are rather stable. We also note that the one-nucleon induced NMWD proceeds with a large weight through the parity-violating "$({}^3S_1)_{\Lambda N} \to ({}^1P_1)_{NN}$ plus $({}^3S_1)_{\Lambda N} \to ({}^3P_1)_{NN}$" channels.

Second, we have clarified the interesting roles and properties of weak decay two-body transition potentials underlying the theory–experiment comparison. It is remarkable to find that the decay potentials based on the non-strange meson (π, ρ, σ, a_1) exchanges and those based on the strange meson (K, K^*, κ, K_1) exchanges show characteristic and intriguing behaviors depending on the decay channels. The roles of various meson exchanges are clarified and summarized as follows:

(1) The potentials due to the (π, ρ, a_1) exchanges have signs opposite to and tend to cancel the potentials due to the corresponding (same $J^{\rm PC}$) (K, K^*, K_1) exchanges in the PC central ${}^1S_0 \to {}^1S_0$ and ${}^3S_1 \to {}^3S_1$ channels and in the tensor ${}^3S_1 \to {}^3D_1$ channel. The two potentials of the σ exchange and the κ exchange have the opposite sign in the ${}^1S_0 \to {}^1S_0$ channel but the same sign in the ${}^3S_1 \to {}^3S_1$ one owing to the isospin dependence of the κ-exchange potential in the final NN state.
(2) In the PV ${}^3S_1 \to {}^1P_1$ channel the potentials of all meson exchanges regardless of the strangeness work additively in the positive sign, and in the PV ${}^3S_1 \to {}^3P_1$ channel the potentials of the (π, σ) exchanges and those of the (K, κ) exchanges work together in the negative sign.
(3) The pomeron exchange potential has a role to reduce the strength of the scalar–isoscalar σ exchange potential, which is necessary to solve the magnitude and sign problem of the decay asymmetries of the emitted protons from the polarized hypernuclei.

Third, we emphasize the following potential properties obtained as a consequence of the corresponding meson exchanges mentioned above. The total central potential in the $({}^1S_0)_{\Lambda N} \to ({}^1S_0)_{NN}$ channel becomes strong and negative. On the other hand, the potential in the $({}^3S_1)_{\Lambda p} \to ({}^3S_1)_{np}$ channel becomes weak and positive, and the total tensor potential in the $({}^3S_1)_{\Lambda p} \to ({}^3D_1)_{np}$ channel

becomes positive and weaker in comparison with the one-pion exchange potential. The parity-violating potentials are totally strong in the $({}^3S_1)_{\Lambda p} \to ({}^1P_1)_{np}$ and $({}^3S_1)_{\Lambda N} \to ({}^3P_1)_{NN}$ channels. These potential characteristics coming from exchanges of mesons and pomeron are newly recognized in this paper. We note that these potential properties constitute the reason why the present extended meson exchange model can explain the experimental decay observables satisfactorily.

As an additional remark, we found that the major part of the present model can be approximated by the potentials due to the limited exchanges of pseudoscalar, vector, and scalar mesons plus pomeron exchange. This is owing to the fact that the axial-vector meson exchange potentials have only a minor effect on the NMWD because of the mutual cancellations among those for the a_1 and K_1 exchanges. This recognition of the role of the axial-vector meson exchange has been altered from our previous works [10,26], in which the a_1 meson has been solely considered as the axial-vector meson.

Further refinement of the model is needed, especially for the treatment of the short-range part of the initial ΛN state, and also the final outgoing NN state. The two-nucleon induced decay rates Γ_{2N} are still an open problem to be studied.

Acknowledgements

We are grateful to Prof. T. Ueda for cooperation in the early stage of this work. Stimulating discussions with and comments by Prof. Y. Yamamoto and Prof. E. Hiyama have been very helpful. One of the authors (K. I.) would like to thank Prof. K. Nakazawa for the warm hospitality at Gifu University.

Appendix A. Expression for Γ_1

Γ_1 is expressed as follows in the shell model framework by using the Block–Dalitz two-body transition amplitudes [39] a, b, c, d, e, and f of $\Lambda p \to np$, when it is assumed that the weak decays take place from the Λ-proton relative S-state ($\hat{J} \equiv \sqrt{2J+1}$):

$$
\begin{aligned}
\Gamma_1 = {} & \frac{4M_N}{2J_H+1}\frac{3}{J_H+1}\sum_{J_1'M_1'\alpha_1'}\sum_{T_1'M_{T_1}'}\sum_{J_2M_2}\sum_{J_{22}}\sum_{M_{H_0}>0}\sum_{n_a\ell_a j_a}\sum_{n_a'\ell_a' j_a'} 2\int d(\cos\theta_{k_1})d\phi_{k_1} \\
& \times \int_0^{k_{2,\max}} dk_2 \frac{(A-2)k_1^2k_2^2}{\sqrt{(A-1)(A-2)k_Q^2 - k_2^2[(A-1)^2-\cos^2\theta_{k_1}]}} \\
& \times (T_1'M_{T_1}'1/2\nu_p|T_HM_{T_H})^2\,(-1)^{\ell_a+j_a+j_\Lambda}(-1)^{\ell_a'+j_a'+j_\Lambda} \\
& \times \mathcal{S}^{1/2}_{J_cT_c,J_1'T_1'\alpha_1'}(j_a,t_N=1/2)\mathcal{S}^{1/2}_{J_cT_c,J_1'T_1'\alpha_1'}(j_a',t_N=1/2) \\
& \times \hat{J}_c\hat{J}_2\,W(J_1'j_aJ_Hj_\Lambda\,;\,J_cJ_2)\cdot\hat{J}_c\hat{J}_{22}\,W(J_1'j_a'J_Hj_\Lambda\,;\,J_cJ_{22}) \\
& \times (J_1'M_1'J_2M_2|J_HM_{H_0})(J_1'M_1'J_{22}M_2|J_HM_{H_0})\cdot M_{H_0} \\
& \times \sum_{L=\ell_a}\sum_{L'=\ell_a'}\sum_{nN}\sum_{n'N'}\sum_{n_\Lambda n_\Lambda'}(-1)^{L-\lambda}M_{\lambda=\ell_a=L}(n_a\ell_an_\Lambda 0\,;\,n0NL\,;\,M_N,M_\Lambda)\,c(n_\Lambda) \\
& \times (-1)^{L'-\lambda'}M_{\lambda'=\ell_a'=L'}(n_a'\ell_a'n_\Lambda' 0\,;\,n'0N'L'\,;\,M_N,M_\Lambda)\,c(n_\Lambda') \\
& \times (-1)^{N+N'}(-i)^{L-L'}\phi_{N,L=\ell_a}(K,b_K)\,\phi_{N'L'=\ell_a'}(K,b_K) \\
& \times \Bigg[\hat{j_a}\cdot 1\,W(j_a\ell_a1/2S=0\,;\,1/2J_2)\cdot\hat{j_a'}\sqrt{3}\,W(j_a'\ell_a'1/2S'=1\,;\,1/2J_{22}) \\
& \times \sum_{\mathcal{M}'}\sum_{MM'}(\mathcal{J}=00LM|J_2M_2)(\mathcal{J}'=1\mathcal{M}'L'M'|J_{22}M_2)(-1)^{M_2}
\end{aligned}
$$

$$
\begin{aligned}
&\times \sqrt{1}\,(\mathcal{J}=00\mathcal{J}'=1-\mathcal{M}'|k=1-\mathcal{M}')\\
&\times \sum_{L_0}\frac{\hat{L}\,\hat{L}'}{\sqrt{4\pi}\,\hat{L}_0}\,(LML'-M'\,|\,L_0\,M-M')\,(L0L'0\,|\,L_00)\\
&\times (-1)^{k=1}\,2\frac{2}{\sqrt{4\pi}}\mathrm{Re}\left\{[ae^*-b(c-\sqrt{2}d)^*/\sqrt{3}]\,Y_{k=1,0-\mathcal{M}'}(\theta_k,\phi_k=0)\right.\\
&\left.\times\, Y_{L_0,M-M'}(\theta_K,\phi_K=0)\right\}\\
&+\hat{j_a}\sqrt{3}\,W(j_a\ell_a1/2S=1\,;\,1/2J_2)\cdot\hat{j'_a}\sqrt{3}\,W(j'_a\ell'_a1/2S'=1\,;\,1/2J_{22})\\
&\times\sum_{\mathcal{M}\mathcal{M}'}\sum_{MM'}(\mathcal{J}=1\mathcal{M}LM|J_2M_2)(\mathcal{J}'=1\mathcal{M}'L'M'|J_{22}M_2)(-1)^{M_2}\\
&\times\sqrt{3}\,(\mathcal{J}=1\mathcal{M}\mathcal{J}'=1-\mathcal{M}'|k=1\mathcal{M}-\mathcal{M}')\\
&\times\sum_{L_0}\frac{\hat{L}\hat{L}'}{\sqrt{4\pi}\,\hat{L}_0}\,(LML'-M'\,|\,L_0\,M-M')\,(L0L'0\,|\,L_00)\\
&\times(-1)^{k=1}\left(-\sqrt{\frac{2}{3}}\right)\frac{2}{\sqrt{4\pi}}\mathrm{Re}\left\{[f(\sqrt{2}c+d)^*]\,Y_{k=1,\mathcal{M}-\mathcal{M}'}(\theta_k,\phi_k=0)\right.\\
&\left.\times\, Y_{L_0,M-M'}(\theta_K,\phi_K=0)\right\}\Big].
\end{aligned}
\tag{A.1}
$$

Appendix B. Meson-decay coupling interactions

The meson-decay Hamiltonians used in this work are as follows (see, e.g., Ref. [10]):

$$\mathcal{H}_{\pi\pi\sigma}=+g_{\pi\pi\sigma}\,\phi_\sigma(\boldsymbol{\varphi}_\pi\cdot\boldsymbol{\varphi}_\pi)+\text{h.c.},\tag{B.1a}$$

$$\mathcal{H}_{\pi\pi\rho}=+g_{\pi\pi\rho}\,\boldsymbol{\phi}^\mu_\rho\cdot\left[(\partial_\mu\boldsymbol{\varphi}_\pi)\times\boldsymbol{\varphi}_\pi-\boldsymbol{\varphi}_\pi\times(\partial_\mu\boldsymbol{\varphi}_\pi)\right]+\text{h.c.},\tag{B.1b}$$

$$\mathcal{H}_{\rho\pi a_1}=+g_{\rho\pi a_1}\,\boldsymbol{\phi}^\mu_{a_1}\cdot(\boldsymbol{\phi}_{\rho,\mu}\times\boldsymbol{\varphi}_\pi)+\text{h.c.},\tag{B.1c}$$

$$\mathcal{H}_{\sigma\pi a_1}=+g_{\sigma\pi\ a_1}\,\boldsymbol{\phi}^\mu_{a_1}\cdot\left[(\partial_\mu\phi_\sigma)\boldsymbol{\varphi}_\pi-\phi_\sigma(\partial_\mu\boldsymbol{\varphi}_\pi)\right]+\text{h.c.},\tag{B.1d}$$

$$\mathcal{H}_{K^*\pi K_1}=+ig_{K^*\pi K_1}\,((\phi^\mu_{K_1})^\dagger\boldsymbol{\tau}\phi_{K^*,\mu})\cdot\boldsymbol{\varphi}_\pi+\text{h.c.},\tag{B.1e}$$

$$\mathcal{H}_{K\pi\kappa}=+g_{K\pi\kappa}\,((\phi^\mu_\kappa)^\dagger\boldsymbol{\tau}\phi_{K,\mu})\cdot\boldsymbol{\varphi}_\pi+\text{h.c.},\tag{B.1f}$$

$$\mathcal{H}_{\pi\pi P}=+g_{\pi\pi P}\,\phi_P(\boldsymbol{\varphi}_\pi\cdot\boldsymbol{\varphi}_\pi)+\text{h.c.}\tag{B.1g}$$

In order to compare the strong meson decay couplings with the literature, e.g. Ref. [72], we define the alternative dimensionless couplings by the Lagrangians

$$\mathcal{L}_{\pi\pi\sigma}=+\frac{1}{2}g'_{\pi\pi\sigma}\,m_\pi\,\phi_\sigma(\boldsymbol{\varphi}_\pi\cdot\boldsymbol{\varphi}_\pi)+\text{h.c.},\tag{B.2a}$$

$$\mathcal{L}_{\pi\pi\rho}=-g'_{\pi\pi\rho}\,\boldsymbol{\phi}^\mu_\rho\cdot(\boldsymbol{\varphi}_\pi\times\overleftrightarrow{\partial_\mu}\boldsymbol{\varphi}_\pi)+\text{h.c.},\tag{B.2b}$$

$$\mathcal{L}_{\rho\pi a_1}=-g'_{\rho\pi a_1}\,M\,\boldsymbol{\phi}^\mu_{a_1}\cdot(\boldsymbol{\varphi}_\pi\times\boldsymbol{\phi}_{\rho,\mu})+\text{h.c.},\tag{B.2c}$$

$$\mathcal{L}_{\sigma\pi a_1}=-g'_{\sigma\pi\ a_1}\,\boldsymbol{\phi}^\mu_{a_1}\cdot(\boldsymbol{\varphi}_\pi\overleftrightarrow{\partial_\mu}\phi_\sigma)+\text{h.c.},\tag{B.2d}$$

$$\mathcal{L}_{K^*\pi K_1}=+ig'_{K^*\pi K_1}\,M\,((\phi^\mu_{K_1})^\dagger\boldsymbol{\tau}\phi_{K^*,\mu})\cdot\boldsymbol{\varphi}_\pi+\text{h.c.},\tag{B.2e}$$

$$\mathcal{L}_{K\pi\kappa} = +g'_{K\pi\kappa}\, M\, ((\phi^{\mu}_{\kappa})^{\dagger}\boldsymbol{\tau}\phi_{K,\mu})\cdot\boldsymbol{\varphi}_{\pi} + \text{h.c.}, \tag{B.2f}$$

$$\mathcal{L}_{\pi\pi P} = +\frac{1}{2}g'_{\pi\pi P}\, M\, \phi_P(\boldsymbol{\varphi}_{\pi}\cdot\boldsymbol{\varphi}_{\pi}) + \text{h.c.}, \tag{B.2g}$$

where we use as scaling masses $m_{\pi} = 140\,\text{MeV/c}^2$ and $M = 938.27\,\text{MeV/c}^2$. In contrast to some of the couplings in Eqs. (B.1a)–(B.1g), the couplings in Eqs. (B.2a)–(B.2g) are all dimensionless. The relation between the couplings of Eqs. (B.1a)–(B.1g) and (B.2a)–(B.2g) can be read off readily, and have a relative minus sign.

The numerical (rationalized) values of the couplings in Eqs. (B.2a)–(B.2g), using Table 1 are:

$$\begin{aligned} g'_{\pi\pi\sigma}/\sqrt{4\pi} &= 7.455, g'_{\pi\pi P}/\sqrt{4\pi} = 2.574, \\ g'_{\pi\pi\rho}/\sqrt{4\pi} &= 1.664, g'_{\rho\pi a_1}/\sqrt{4\pi} = 0.499, \\ g'_{\sigma\pi a_1}/\sqrt{4\pi} &= 1.634, g'_{K^*\pi K_1}/\sqrt{4\pi} = 1.153, \\ g'_{K\pi\kappa}/\sqrt{4\pi} &= 0.704. \end{aligned} \tag{B.3}$$

References

[1] H. Bandō, Prog. Theor. Phys. Suppl. **81**, 181 (1985).
[2] H. Bandō, T. Motoba, and J. Žofka, Int. J. Mod. Phys. A **5**, 4021 (1990).
[3] O. Hashimoto and T. Tamura, Prog. Part. Nucl. Phys. **57**, 564 (2006).
[4] E. Botta, T. Bressani, S. Bufalino, and A. Feliciello, Riv. Nuovo Cim. **38**, 384 (2015).
[5] A. Gal, E. V. Hungerford, and D. J. Millener, Rev. Mod. Phys. **88**, 035004 (2016).
[6] H. Ejiri, T. Kishimoto, and H. Noumi, Phys. Lett. B **225**, 35 (1989).
[7] K. Itonaga, T. Motoba, O. Richter, and M. Sotona, Phys. Rev. C **49**, 1045 (1994).
[8] K. Itonaga, T. Motoba, and M. Sotona, Prog. Theor. Phys. Suppl. **117**, 17 (1994).
[9] T. Motoba, K. Itonaga, and H. Bandō, Nucl. Phys. A **489**, 683 (1988).
[10] K. Itonaga and T. Motoba, Prog. Theor. Phys. Suppl. **185**, 252 (2010).
[11] W. M. Alberico and G. Garbarino, Phys. Rep. **369**, 1 (2002).
[12] T. Nagae, Prog. Theor. Phys. Suppl. **185**, 299 (2010).
[13] M. Agnello et al. [FINUDA Collaboration], Phys. Lett. B **738**, 499 (2014).
[14] E. Botta, T. Bressani, S. Bufalino, and A. Feliciello, Phys. Lett. B **748**, 86 (2015).
[15] C. Rappold et al., Phys. Lett. B **728**, 543 (2014) and references therein.
[16] T. R. Saito et al., Nucl. Phys. A **954**, 199 (2016) and references therein.
[17] Y. Xu for the STAR Collaboration, JPS Conf. Proc. **17**, 021005 (2017).
[18] J. Adam et al. [ALICE Collaboration], Phys. Lett. B **754**, 360 (2016).
[19] J. B. Adams, Phys. Rev. **156**, 1611 (1967).
[20] B. H. J. McKellar and B. F. Gibson, Phys. Rev. C **30**, 322 (1984).
[21] A. Parreño, A. Ramos, and C. Bennhold, Phys. Rev. C **56**, 339 (1997).
[22] A. Parreño and A. Ramos, Phys. Rev. C **65**, 015204 (2002).
[23] C. Chumillas, G. Garbarino, A. Parreño, and A. Ramos, Phys. Lett. B **657**, 180 (2007).
[24] D. Jido, E. Oset, and J. E. Palomar, Nucl. Phys. A **694**, 525 (2001).
[25] K. Itonaga, T. Ueda, and T. Motoba, Phys. Rev. C **65**, 034617 (2002).
[26] K. Itonaga, T. Motoba, T. Ueda, and Th. A. Rijken, Phys. Rev. C **77**, 044605 (2008).
[27] K. Sasaki, T. Inoue, and M. Oka, Nucl. Phys. A **707**, 477 (2002).
[28] K. Sasaki, M. Izaki, and M. Oka, Phys. Rev. C **71**, 035502 (2005).
[29] A. Parreño, C. Bennhold, and B. R. Holstein, Phys. Rev. C **70**, 051601(R) (2004).
[30] A. Parreño, C. Bennhold, and B. R. Holstein, Nucl. Phys. A **754**, 127 (2005).
[31] Th. A. Rijken, M. M. Nagels, and Y. Yamamoto, Prog. Theor. Phys. Suppl. **185**, 14 (2010).
[32] M. M. Nagels, Th. A. Rijken, and Y. Yamamoto, http://nn-online.org/eprints/pdf/16.01.pdf (date last accessed November 7, 2018).

[33] M. M. Nagels, Th. A. Rijken, and Y. Yamamoto, http://nn-online.org/eprints/pdf/16.02.pdf (date last accessed November 7, 2018).
[34] X. Qiu et al. [HKS (JLab E02-017) Collaboration], Nucl. Phys. A **973**, 116 (2018).
[35] N. Austern, *Direct Nuclear Reaction Theories* (Wiley-Interscience, New York, 1970).
[36] G. R. Satchler, *Direct Nuclear Reactions* (Clarendon Press, Oxford, 1983).
[37] A. Ramos, E. van Meijgaard, C. Bennhold, and B. K. Jennings, Nucl. Phys. A **544**, 703 (1992).
[38] C. Barbero, A. P. Galeão, and F. Krmpotić, Phys. Rev. C **72**, 035210 (2005).
[39] M. M. Block and R. H. Dalitz, Phys. Rev. Lett. **11**, 96 (1963).
[40] M. M. Nagels, T. A. Rijken, and J. J. de Swart, Phys. Rev. D **17**, 768 (1978).
[41] Th. A. Rijken, Phys. Rev. C **73**, 044007 (2006).
[42] M. M. Nagels, T. A. Rijken, and J. J. de Swart, Phys. Rev. D **12**, 744 (1975).
[43] M. M. Nagels, T. A. Rijken, and J. J. de Swart, Phys. Rev. D **15**, 2547 (1977).
[44] T. Ueda, F. E. Riewe, and A. E. S. Green, Phys. Rev. C **17**, 1763 (1978).
[45] K. Tominaga and T. Ueda, Nucl. Phys. A **693**, 731 (2001).
[46] T. E. O. Ericson and W. Weise, *Pions and Nuclei* (Clarendon Press, Oxford, 1988).
[47] S. Ajimura et al., Phys. Rev. Lett. **84**, 4052 (2000).
[48] T. Maruta et al., Nucl. Phys. A **754**, 168 (2005).
[49] T. Maruta, Ph.D. thesis, KEK Report 2006-1, 2006.
[50] H. Outa, M. Aoki, R. S. Hayano, T. Ishikawa, M. Iwasaki, A. Sakaguchi, E. Takada, H. Tamura, and T. Yamazaki, Nucl. Phys. A **639**, 251c (1998).
[51] H. Outa, M. Aoki, R. S. Hayano, T. Ishikawa, M. Iwasaki, A. Sakaguchi, E. Takada, H. Tamura, and T. Yamazaki, Nucl. Phys. A **585**, 109 (1995).
[52] V. J. Zeps, Nucl. Phys. A **639**, 261c (1998).
[53] J. D. Parker et al., Phys. Rev. C **76**, 035501 (2007).
[54] H. Outa et al., Nucl. Phys. A **754**, 157 (2005).
[55] B. H. Kang et al., Phys. Rev. Lett. **96**, 062301 (2006).
[56] J. J. Szymanski et al., Phys. Rev. C **43**, 849 (1991).
[57] H. Noumi, S. Ajimura, H. Ejiri, A. Higashi, T. Kishimoto, D. R. Gill, L. Lee, A. Olin, T. Fukuda, and O. Hashimoto, Phys. Rev. C **52**, 2936 (1995).
[58] H. Noumi et al., in *Proc. IVth Int. Symp. on Weak and Electromagnetic Interactions in Nuclei*, eds. H. Ejiri, T. Kishimoto, and T. Sato (World Scientific, Singapore, 1995), p. 550.
[59] Y. Sato et al., Phys. Rev. C **71**, 025203 (2005).
[60] M. J. Kim et al., Phys. Lett. B **641**, 28 (2006).
[61] M. Kim et al., Phys. Rev. Lett. **103**, 182502 (2009).
[62] H. Bhang et al., Korean Phys. Soc. **59**, 1461 (2011).
[63] T. Motoba, K. Itonaga, and H. Bandō, Nucl. Phys. A **489**, 683 (1988).
[64] T. Motoba and K. Itonaga, Prog. Theor. Phys. Suppl. **117**, 477 (1994).
[65] S. Kameoka et al., Nucl. Phys. A **754**, 173 (2005).
[66] R. Grace et al., Phys. Rev. Lett. **55**, 1055 (1985).
[67] H. Park et al., Phys. Rev. C **61**, 054004 (2000).
[68] H. C. Bhang et al., Phys. Rev. Lett. **81**, 4321 (1998).
[69] H. C. Bhang et al., Nucl. Phys. A **639**, 269c (1998).
[70] K. J. Nield, T. Bowen, G. D. Cable, D. A. DeLise, E. W. Jenkins, R. M. Kalbach, R. C. Noggle, and A. E. Pifer, Phys. Rev. C **13**, 1263 (1976).
[71] J. P. Bocquet et al., Phys. Lett. B **192**, 312 (1987).
[72] M. M. Nagels, Th. A. Rijken, J. J. De Swart, G. C. Oades, J. L. Petersen, A. C. Irving, C. Jarlskog, W. Pfeil, H. Pilkuhn, and H. P. Jakob, Nucl. Phys. B **147**, 189 (1979).